Multi-directional Schlieren 3D-CT measurements validation of a circular supersonic micro-nozzle operating at underexpanded condition using WENO numerical method

Master's Thesis

Master of Science in Aeronautical Engineering

Author:

Juan Jose Robles Solano

Tutors:

Yojiro Ishino (NIT)

Sergio Hoyas Calvo (UPV)

Nagoya, at 11th of June, 2018

Acknowledgements

Abstract

In the present world exits a tendency to the optimization of the different functions of a system in order to make the most of the expended energy and save resources. The project developed by the department of *Mechanical Engineering* of the *Nagoya Institute of Technology* consist of using an innovative multi-directional Schlieren quantitative system to understand the performance of flow fields with density gradients. The objective is to develop a trustworthy method to measure complex flows structure which are impossible to study analytically and to verify numerical methods.

The experimental method consists of two different phases. The first part is the measurement of the target using the multi-directional quantitative Schlieren system. 20 measurements are done simultaneously, each one at a different direction. Secondly, the "density thickness images" can be obtained and used in 3D-CT reconstruction to obtain the 3D density field.

The present project is focused on the measurement of exhaust gases of a supersonic axisymmetric micro-nozzle with circular cross-section working at slightly underexpanded condition ($JPR > 1$). Three measurements at different initial conditions are analyzed ($NPR\ 4, 4.5\ and\ 5$).

A well-known numerical method who solve Euler equations have been implemented to verify the validity of the present experimental procedure. Euler equations are a set of hyperbolic equations which govern adiabatic and inviscid flow. Therefore, they can be used to solve the flow of a micro-nozzle working at underexpanded condition. The numerical method uses the high-order weighted essentially non-oscillatory (WENO) finite differences scheme with fifth-order-accurate for spatial discretization and fourth-order-accurate Runge-Kutta scheme for time integration. The validity of this method has been checked with the experimental data provided by (Seiner & Norum, 1979). Afterward, the numerical method is solved using our initial conditions and a comparation of the results are done.

Nomenclature

ºC	Celsius degrees
a	Displacement at the cut-off
a_{sp}	Sonic speed
A^*	Area at the nozzle throat
A_e	Area at the nozzle exist
B_n	Brightness without knife
c	Speed of the light in vacuum
DBP	Distributed back projection
D_j	Fully expanded jet diameter
EM	Expectation Maximization
f_c	Focal length of the focusing lens
fps	Frames per second
jpg	Joint Photographic Experts Group
JPR	Jet Pressure Ratio
K	Kelvin
Kg	Kilograms
K_{GD}	Gladstone-Dale constant
kPa	Kilopascals
MAP	Maximum a posteriori
M_d	Nozzle design Mach number
M_j	Fully expended Mach
ML	Maximum Likelihood
ML-EM	Maximum Likelihood-Expectation Maximization
mm	Millimeters
MPa	Megapascals
ms	Milliseconds
n	Refractive index
NPR	Nozzle Pressure Ratio
P_0	Absolute (stagnation) pressure
P_G	Gauge pressure
P_b	Back (ambient) pressure
P_e	Exit pressure
png	Portable Network Graphics
RGB	Red, green and blue
s	Path of the light ray
T_0	Absolute (stagnation) temperature
T_b	Ambient temperature
u_e	Jet exit axial velocity
v	Velocity of the light in the medium
λ_m	Bessel zeros
ρ_0	Absolute (stagnation) density
ρ_b	Back (ambient) density
ρ_e	Jet exit density
ρ_j	Fully expanded et density
ΔB	Deviation brightness on Schlieren image
Δa	The resulting displacement at the cut-off

D	Nozzle exit diameter
Dt	Density thickness
J	Bessel function
M	Mach number
γ	Specific heat ratio
θ	Incidence angle
μm	Micrometers
μs	Microseconds

Table of contents

Table of Figures

Table of Tables

1. Introduction

1.1. Motivation

In daily life, we usually face with flows where the density is not uniform. This can be observed in combustion and in some compressible flow movements, such as flows working at supersonic condition. The physical equations which define these phenomena are partial differential equations system (Navier-Stokes equations for Newtonian flows) which are impossible to solve analytically with the present mathematic techniques. For this reason, these physical phenomena are described using experimental techniques and numerical method.

Experimental techniques and numerical approaches for solving physical phenomena always work together. On the one hand, using exclusively experimental techniques to solve all the cases of the study could be extremely expensive. Therefore, some numerical model is needed to reduce the expenses. On the other hand, in order to create a numerical method, many simplifications are done to the real equations which can affect to the final solution. For that, some experimental results are needed to contrast the solution of the numerical model with real data.

An innovative quantitative Schlieren system with 20 cameras at 20 different direction is used to measure combustion flames at (Ishino, et al., 2016), (Ishino, et al., 2015), (Ishino, Horimoto, Kato, Ishiguro, & Saiki, 2013) and (Nazari A. Z., et al., 2017). Schlieren technique have been proved to be a versatile tool to see the density variation of flow at combustion and supersonic condition. (Nazari A. , 2017) and (Nazari A. Z., et al., 2017) used this innovative system to measure the exhaust gases of a supersonic micro-nozzle working at supersonic condition. The goal is to characterize the flow of different micro-nozzles with different cross-sections, which can operate in different auxiliary system, such as in satellites or missile orientation systems.

1.2. Objective

The main objective of the present project is to create a model which can predict the performance of an underexpanded supersonic jet. The model will be based on Euler equations which will be solved using a numerical method based on WENO for spatial discretization and Runge-Kutta 4 step for time integration. Software used in the present study are MATLAB® and FORTRAN® to implement the code, and PAINTSHOP® to process the different data obtained with the Schlieren system. The present study is divided in 3 different Section:

- Section 2: in this section all the background knowledge needed to understand the present project is explained. It is divided in 3 different subsections. The first subsection contains the information related to the characterization of a nozzle flow and the basic scheme of the numerical approach used to simulate the flow. The second subsection includes the basic physic of the Schlieren method. Finally, the last subsection explains the ML-EM method used in computer tomography (3D-CT) reconstruction, used to obtain 3D data of the jet.
- Section 3: the experimental method carried out to measure the supersonic micro-jet is fully explained in this section, as well as the process to obtain the 3D-CT reconstruction of the experimental data.
- Section 4: the results of the numerical model and the experimental measurements are presented. Firstly, the numerical method is validated with data from (Cheng & Lee, 2005). After that, the experimental results are compared with the measurements in radial and axial direction.

1.3. Methodology

The present project was created due to the need of developing a model which was able to characterize the supersonic flow of a jet working at underexpanded condition. Several experiments have been carried out to measure the performance of a supersonic micro-nozzle with circular cross-section. However, it is impossible to study all the cross-section shape and all the experimental setting. For all that, a model has been implemented with the objective to reduce the expenses and the time of the experimental procedure, and for the ability to remove not promising experimental setting.

The present study is focused on the implementation of a numerical method which will be able to simulate the circular nozzle presented in Section 3.1. Several numerical method are proposed to solve the present problem: TAM model by (Jackson & Tam, 1985), $k\epsilon$ by (Dash, Wolf, & Seiner, 1985), (Chen, 1998) and WENO method (Cheng & Lee, 2005). The numerical method which our software and hardware tools allow us to compute is (Cheng & Lee, 2005). Therefore, this is the method developed in the following sections.

Before applying the WENO method to our experimental data, the model is validated using three different approach: Prandtl model explained by (Jackson & Tam, 1985), the nozzle simulation presented by (Cheng & Lee, 2005) and the experimental measures carried out by (Seiner & Norum, 1979). Once the model is validated we can process to compare the results with our experimental results.

Regarding the experimental results, three different measurements have been obtained for underexpanded condition with NPR equal to 4, 4.5 and 5. All the data have been processed and the density is obtained. At that point, both experimental and numerical solutions can be compared and conclusion of the results can be exposed.

2. Theoretical background

2.1. Nozzle flow

The flow which goes through the nozzle is compressible, hence the density value change in the different points of the flow structure. The consequence of working with compressible flow is that density is variable and requires more elaboration (Bernoulli's equation (Eq. 2.1) cannot be used since density is not constant).

$$p + \frac{1}{2}\rho V^2 = const$$

Eq. 2.1

2.1.1. Isentropic relations

Since it is not possible to use Eq. 2.1 to analyze a compressible flow, it is needed to use another approach. Isentropic relations are frequently used in the analysis of compressible flows. They relate pressure, density and temperature (Eq. 2.2)[1].

$$\frac{P_2}{P_1} = \left(\frac{\rho_2}{\rho_1}\right)^{\gamma} = \left(\frac{T_2}{T_1}\right)^{\frac{\gamma}{\gamma-1}}$$

Eq. 2.2

Where p_i is the pressure at one fluid point, T_i is the temperature and ρ_i is the density. γ is defined as the specific heat ratio which can be considered 1.4 in the air.

An isentropic process is defined as adiabatic and reversible. For an adiabatic process, the heat transfer is null ($\delta q = 0$), and for a reversible process, the entropy is also null ($\delta s = 0$) (Anderson, 1982). Even though Eq. 2.2 seems very restrictive (adiabatic and reversible), the fluid elements outside the boundary layer are experiencing this process. At these points, dissipative effects are negligible.

The present study is focused on the study of micro-nozzles with circular cross-section. These nozzles are axisymmetric and have a convergent-divergent (Laval) shape. Figure 2.1 represent a convergent-divergent nozzle scheme, where the flows move from left to right. As the flow moves forward inside the nozzle, its speed increases whereas its pressure and temperature decrease.

The convergent-divergent nozzle can be divided in three parts. The Mach number ($M = u_e/a_{sp}$) is the parameter which define this process and it can be defined as the velocity of the flow over it sonic speed.

- Convergent: in this section of the nozzle, the flow moves at subsonic speed ($M < 1$) and it is accelerated until sonic speed. At subsonic condition, when the area is reduced, the speed of the flow rise up.
- Throat: the flow meets sonic condition ($M = 1$). At this point, the area of the cross-section is the smallest of the nozzle.
- Divergent: in this section of the nozzle, the flows move at supersonic speed ($M > 1$). At supersonic condition when the area is augmented, the speed of the flow rise.

---

[1] Eq. 2.2 is calculated from the 1st and 2nd laws of the thermodynamic. The development of this equation is fully detailed in Section 1.4 of (Anderson, 1982).
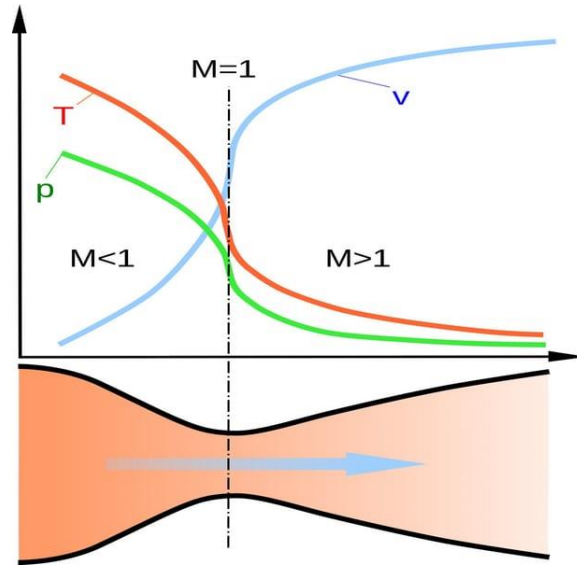
Figure 2.1. Convergent-divergent nozzle diagram.

Making use of the energy equation[2] and Eq. 2.2 it is possible to obtain the pressure, temperature and density at any point of the nozzle as a function of the Mach and the stagnation condition. The subscript 0 represent the stagnation condition.

$$\frac{P_0}{P} = \left[1 + \frac{1}{2}(\gamma - 1)M^2\right]^{\frac{\gamma}{\gamma-1}}$$

Eq. 2.3

$$\frac{\rho_0}{\rho} = \left[1 + \frac{1}{2}(\gamma - 1)M^2\right]^{\frac{1}{\gamma-1}}$$

Eq. 2.4

$$\frac{T_0}{T} = \left[1 + \frac{1}{2}(\gamma - 1)M^2\right]^{\frac{\gamma}{\gamma-1}}$$

Eq. 2.5

The design Mach number (M_d) at the exit is related with the ratio of the exit area (A_e) over the throat area (A^*). Eq. 2.6 shows this relation.

$$\frac{A_e}{A^*} = \frac{1}{M_d}\left(\frac{1 + \frac{1}{2}(\gamma - 1)M_d^2}{\frac{1}{2}(\gamma + 1)}\right)^{\frac{\gamma+1}{2(\gamma-1)}}$$

Eq. 2.6

If the M_d is replaced by the fully expanded jet Mach number (M_j) the ratio obtained in Eq. 2.7 is the fully expanded jet cross-section (A_j) over A^*.

---

[2] The calculation of Eq. 2.3 Eq. 2.4 and Eq. 2.5 is detailed in Section 3.5 of (Anderson, 1982).

$$\frac{A_j}{A^*} = \frac{1}{M_j}\left(\frac{1 + \frac{1}{2}(\gamma - 1)M_j^2}{\frac{1}{2}(\gamma + 1)}\right)^{\frac{\gamma+1}{2(\gamma-1)}}$$

Eq. 2.7

Each nozzle is designed to operate at designed condition, at a specific Mach. The parameter which define the working condition is named nozzle pressure ratio (NPR). NPR depends on the ratio of the stagnation pressure (P_0) over the ambient pressure (P_b) (Eq. 2.8).

$$NPR = \frac{P_0}{P_b} = \left[1 + \frac{1}{2}(\gamma - 1)M_j^2\right]^{\frac{\gamma}{\gamma-1}}$$

Eq. 2.8

The designed nozzle pressure ratio (DNPR) is the NPR when the designed conditions are met (Eq. 2.9).

$$DNPR = \frac{P_0}{P_e} = \left[1 + \frac{1}{2}(\gamma - 1)M_d^2\right]^{\frac{\gamma}{\gamma-1}}$$

Eq. 2.9

2.1.2. Supersonic jets

Supersonic jets can operate at three different regimens, depending on the value of the jet pressure ratio (JPR). JPR can be defined as the ratio of the exit pressure (P_e) over the ambient pressure. JPR is defined by Eq. 2.10 which can be obtained dividing Eq. 2.8 into Eq. 2.9.

$$JPR = \frac{P_e}{P_b} = \left[\frac{1 + \frac{1}{2}(\gamma - 1)M_j^2}{1 + \frac{1}{2}(\gamma - 1)M_d^2}\right]^{\frac{\gamma}{\gamma-1}}$$

Eq. 2.10

In addition, an explicit formula of the fully expanded jet diameter (D_j) can be calculated dividing Eq. 2.7 over Eq. 2.6, where D_e is the design diameter of the nozzle.

$$\frac{D_j}{D_e} = \left(\frac{M_d}{M_j}\right)^{\frac{1}{2}}\left(\frac{1 + \frac{1}{2}(\gamma - 1)M_j^2}{1 + \frac{1}{2}(\gamma - 1)M_d^2}\right)^{\frac{\gamma+1}{4(\gamma-1)}}$$

Eq. 2.11

Figure 2.2 shows the three different regimens in which a nozzle can be operated. The pictures have been obtained using 20-directional quantitative Schlieren photography explained in Section 3.

- JPR<1 and $M_j < M_d$ (overexpanded). Off-design operation.
- JPR=1 and $M_j = M_d$ (perfectly-expanded). On-design operation.
- JPR>1 and $M_j > M_d$ (underexpanded). Off-design-operation.

When a nozzle is operating at off-design condition, two different shock patterns in the core region can be observed, which are referred to as overexpanded and underexpanded patterns.

(a) JPR=0.95   (b) JPR=1   (c) JPR=1.36
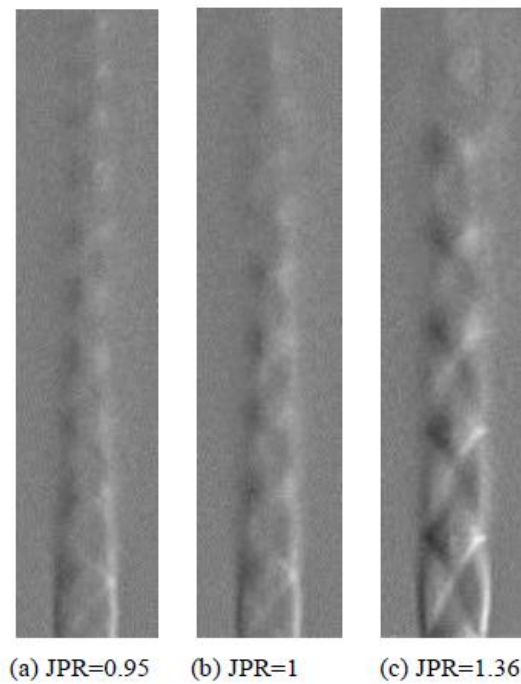
Figure 2.2. Quantitative Schlieren images of overexpanded, perfectly-expanded and underexpanded (from left to right) of supersonic micro-jets (Nazari A. , 2017).

2.1.2.1. Underexpanded supersonic jet

When a nozzle is working at underexpanded condition, a characteristic structure appear at the nozzle exit. Figure 2.3 shows a schematic diagram of this characteristic structure in the left, and on the right, it shows a Schlieren photograph of a real nozzle working at the referred condition.

This axisymmetric structure has several remarkable features. First, the jet boundary oscillates as the jet gas periodically overexpands and compresses in its attempt to match the ambient pressure. The boundary arc communicates to the interior of the jet by sound waves, which, by definition, travel slower than supersonic flow. The characteristic paths of the sound waves converge to form the second remarkable feature of the jet, the network of crisscrossed shock waves, or shock diamonds. These standing shocks alternate with rarefaction fans. The gas in the jet interior expands and cools as it flows through the expansion waves and is compressed and heats as it passes through the shock diamonds. The sequential reflections of the expansion waves and shocks develop shock-cell structure. The positions of greatest gas compression do not coincide with the positions of minimum jet diameter. The streamlines in the figure indicate the flow paths of the gas. The gas bends out toward the boundary as it passes through rarefaction fans and bends back toward the axis as it passes through shock fronts.
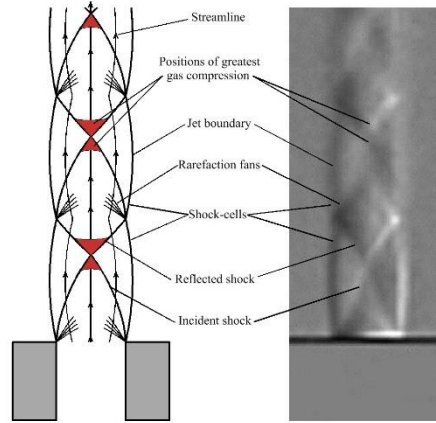
Figure 2.3. Schematic diagram of shock-cell structure (left) and quantitative Schlieren image (right) of supersonic underexpanded jet (Nazari A. , 2017).

2.1.2.2.   Prandtl Model

As starting point for the numerical approach, we are going to introduce an analytical solution for underexpanded jet obtained by Prandtl (Jackson & Tam, 1985). In this treatment, shocks are considered to be small perturbation of a fully expanded supersonic jet. The jet itself is modeled as a uniform column of flow bounded by a vortex sheet. Assuming a small variation of pressure at the nozzle exit (δP), the governing equations are shown in Eq. 2.12.

$$\rho_j \nabla \cdot V_s + U_j \frac{\partial \rho_s}{\partial x} = 0$$

$$\rho_j U_j \frac{\partial V_s}{\partial x} = -\nabla P_s$$

$$P_s = a_j^2 \rho_s$$

Eq. 2.12

Eq. 2.12 represents the linearized continuity, momentum and energy equations for a compressible, inviscid and axisymmetric jet.

The initial conditions are given by:

$$V_s = 0, Ps = \delta P \ for \ r < R_d ; P_s = 0 \ for \ r \geq R_d$$

V_s can be eliminated from Eq. 2.12 and the equation left can be solved by eigenfunction expansion to yield the following solution in the expansion case[3]:

$$P_s = \sum_{m=1}^{\infty} A_m J_0 \left(\frac{\lambda_m r}{R_j} \right) Cos \left(\frac{\lambda_m x}{R_j \left(M_j^2 - 1 \right)^{\frac{1}{2}}} \right)$$

Eq. 2.13

Where

---

[3] In Appendix 3 the code used to simulate Prandtl's model can be found with an example.

$$A_m = \frac{2 \, \delta P \, \frac{R_d}{R_j} \, J_1\left(\frac{\lambda_m R_d}{R_j}\right)}{\lambda_m J_1^2(\lambda_m)}$$

Eq. 2.14

J represents the Bessel function, and λ_m are the increasingly ordered zeros of J_0.

The physical interpretation is that an initial pressure mismatch at the nozzle exit generates a disturbance, which is selectively decomposed into various radial eigenmodes of the jet. The jet then acts as a waveguide directing each component as it propagates downstream within the mean flow.

The two mean limitations of this model are explained below.

1. Prandtl model works accurately only in the immediate vicinity of the nozzle exit where the mixing layer is thin.
2. It does not take into account the turbulence in the mixing layer which trend to decrease the amplitude of the solution.

Moreover, Prandtl took the dominant first term of the Bessel series solution (Powell, 2009), as yielding the fundamental wavelength of the observed periodicity, namely the cell length (Eq. 2.15):

$$L_c = 1.306 \sqrt{M_j^2 - 1}$$

Eq. 2.15
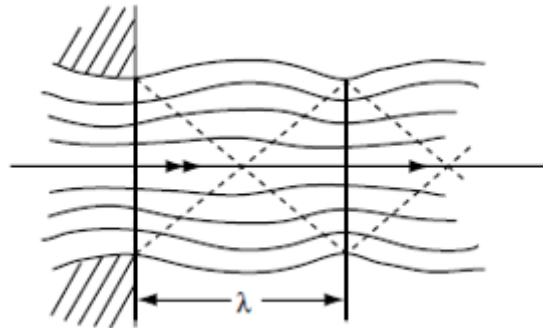
Figure 2.4. Prandtl wavelength representation (Powell, 2009).

Where the constant 1.306 is given as a minor error as it should have been $\pi/2.40483 = 1.306$ as written here, the denominator been the first root of the Bessel function.

Figure 2.4 shows a graphic representation of the definition of cell length. It coincides with the shock cell represented in Figure 2.3 but with a simpler representation since rarefaction fans are not displayed. The shock length includes a rarefaction fan, an incident shock and a reflection shock.

α is defined as the shock wave angle which will emanate from the nozzle exit. According to Mach, it is defined as:

$$\alpha = \arcsin\left(\frac{1}{M}\right)$$

Eq. 2.16

2.1.3. Numerical approach (WENO algorithm)

In the present study, a numerical simulation has been implemented in order to verify the micro-nozzle experimental measurements. The numerical method created uses the high-order weighted essentially non-oscillatory (WENO) finite differences schemes with fifth-order-accurate for spatial discretization and the fourth-order-accurate Runge-Kutta scheme for time integration. This numerical method is called the *Lui, Osher and Chan WENO schemes*, it is fully explained by (Jiang & Shu, 1996) and it is applied to the supersonic jet in (Cheng & Lee, 2005).

2.1.3.1. *Governing equation*

The equations which define the behavior of a supersonic jet without body forces and external heat addition for an inviscid and compressible flow field are the time dependent Euler equations (Eq. 2.17).

$$\frac{\partial W}{\partial t} + \frac{\partial F}{\partial x} + \frac{\partial G}{\partial y} + \alpha S = 0$$

Eq. 2.17

Where $\alpha = 0$ represents 2D planar flow and $\alpha = 1$ represents 2D axisymmetric flow. The flux vectors of Eq. 2.17 are shown in Eq. 2.18.

$$W = \begin{bmatrix} \rho \\ \rho u \\ \rho v \\ e \end{bmatrix}, F = \begin{bmatrix} \rho u \\ \rho u^2 + p \\ \rho uv \\ (e+p)u \end{bmatrix}, G = \begin{bmatrix} \rho v \\ \rho uv \\ \rho v^2 + p \\ (e+p)v \end{bmatrix}, S = \frac{1}{y}\begin{bmatrix} \rho v \\ \rho uv \\ \rho v^2 + p \\ (e+p)v \end{bmatrix}$$

Eq. 2.18

The above governing equations represent the conservation of mass, momentum and total energy for inviscid fluid motion. The variables $\rho, u, v, p, e \text{ and } t$ fully define the state of the fluid at a specific location. These variables are density, axial-velocity, radial-velocity, pressure, total energy per mass unit and time respectively. For an ideal gas, the pressure is related by the equation of state (Eq. 2.19):

$$p = (\gamma - 1)(e - 0.5\rho(u^2 + v^2)$$

Eq. 2.19

$\gamma = 1.4$ is the ratio of specific heats for air.

The equations Eq. 2.17 and Eq. 2.18 has been transformed in term of dimensionless variables using the following scales:

- Spatial scale: diameter (D)
- Velocity scale: axial-velocity at the nozzle exit (u_e)
- Density scale: jet exit density (ρ_e)
- Pressure and energy scale: $\rho_e u_e^2$
- Time scale: D/u_e

2.1.3.2.   Temporal integration (Runge-Kutta)

For the temporal integration using the fourth-order-accurate Runge Kutta (RK4), Eq. 2.17 must be written as Eq. 2.20:

$$\frac{dW}{dt} = L(W) = -\left(F(W)_x + G(W)_y + \alpha S(W)\right)$$

Eq. 2.20

$L(W)$ is defined as a discretization of the spatial operator. Let assume the dependence of $W, x \; and \; y$ is known; therefore, Eq. 2.20 can be solved using RK4 as a regular time dependent differential equation. RK4 method can be written as:

- $W^{(1)} = W^n + \frac{1}{2}\Delta t^n L(W^n)$
- $W^{(2)} = W^n + \frac{1}{2}\Delta t^n L\left(W^{(1)}\right)$
- $W^{(3)} = W^n + \Delta t^n L\left(W^{(2)}\right)$
- $W^{n+1} = \frac{1}{3}\left(-W^n + W^{(1)} + 2W^{(2)} + W^{(3)}\right) + \frac{1}{6}\Delta t^n L\left(W^{(3)}\right)$

The superscript n denotes the time step, $W^{(i)}$ is the intermediate vector and Δt^n is the time increment which is defined as:

$$\Delta t^n = \frac{CFL}{\frac{\max(|u^n|)}{dx} + \frac{\max(|v^n|)}{dy}}$$

Eq. 2.21

It is possible to observe in Eq. 2.21 that the time increment is not constant and it depend on the previous velocity field. CFL is defined as the Courant–Friedrichs–Lewy (CFL) condition for convergence while solving certain partial differential equations. Time step must be less than a certain time, otherwise the simulation produces incorrect results. The CFL number is defined between a range of 0.2 and 0.4.

2.1.3.3.   Spatial discretization

In order to solve Eq. 2.20 using RK4, $L(W)$ must be calculated in each step. It is defined as a discretization of the spatial operator and its expression for each cell of the mesh is shown in Eq. 2.22. The space is divided into uniform interval of size Δx and Δy with $x_i = i\,\Delta x$ and $y_j = j\,\Delta y$.

$$L_{i,j}(W) = -\alpha S_{i,j} - \left[\frac{1}{\Delta x}\left(\tilde{F}_{i+\frac{1}{2},j} - \tilde{F}_{i-\frac{1}{2},j}\right) + \frac{1}{\Delta y}\left(\tilde{G}_{i,j+\frac{1}{2}} - \tilde{G}_{i,j-\frac{1}{2}}\right)\right]$$

Eq. 2.22

$\tilde{F}$ and $\tilde{G}$ denote the interface fluxes in the x and y direction respectively and $S_{i,j}$ is the source term at the grid point. Figure 2.5 shows a scheme of the interface fluxes at a generic cell (i, j) of the mesh. In the scheme, the arrows indicate the positive direction of the fluxes.
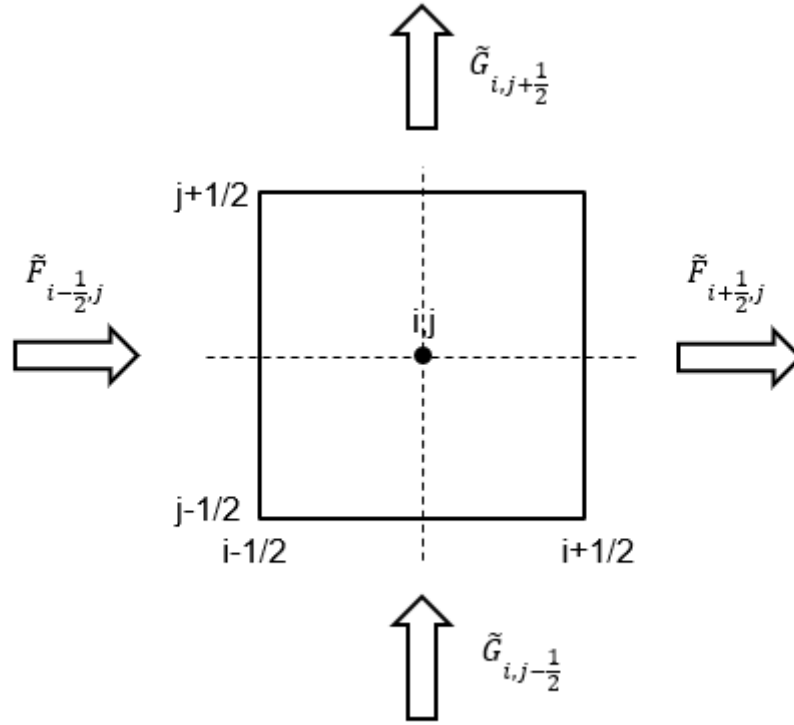
Figure 2.5. Interface fluxes at one cell (i, j) of the spatial discretization.

High-order accuracy distribution is achieved with high-order approximation of the fluxes function at cell interfaces. The flux distribution is going to be developed only for the flux at the x-axis ($\tilde{F}(W)$), but flux at y-axis ($\tilde{G}(W)$) can be computed similarly. The distribution of interpolation points (stencil) is chosen according with the Lax-Friedrichs scheme (Eq. 2.23).

$$\tilde{F}(W) = F^+(W) + F^-(W)$$

Eq. 2.23

Therefore, the flux distribution can be defined as the summation of the positive and negative fluxes interacting with the cells interfaces. These fluxes must satisfy:

- $\dfrac{dF^+}{dW} \geq 0$ for all $F^+(W)$.
- $\dfrac{dF^-}{dW} \leq 0$ for all $F^-(W)$.

One solution to meet the requirements is to use the global Lax-Friedrichs flux splitting (Eq. 2.24)

$$\tilde{F}^\pm(W) = \frac{1}{2}(F(W) \pm \beta W)$$

Eq. 2.24

Where β is defined as the maximum value of the Jacobian matrix of the flux[4].

---

[4] The development of the Jacobian matrix is fully explained in Appendix I.

$$\beta = \max(|J_F(W)|)$$

Therefore, the flux in the interface can be divided into two numerical fluxes:

$$\tilde{F}_{i+\frac{1}{2},j}(W) = \tilde{F}^+_{i+\frac{1}{2},j}(W) + \tilde{F}^-_{i+\frac{1}{2},j}(W)$$

The following explanation is the particularization of WENO method for 5th-order accuracy with $r = 3$, being r the stencil candidates. The generalization of this method can be found in (Jiang & Shu, 1996). Here, we will explain the computation for $\tilde{F}^+_{i+\frac{1}{2},j}$ since the formulas of $\tilde{F}^-_{i+\frac{1}{2},j}$ are symmetric with $x_{i+\frac{1}{2},j}$.

Let's denote the $r = 3$ candidates stencils by $S_k, k = 0, 1, 2$.

$$S_k = S\left(x_{j+k-r+1}, x_{j+k-r+2}, x_{j+k-r+3}\right)$$

The 3 stencils used to obtain the flux at the cell interface are:

$$S_0 = \frac{\left(2\,F_{i-2,j} - 7\,F_{i-1,j} + 11\,F_{i,j}\right)}{6}$$

$$S_1 = \frac{\left(-\,F_{i-1,j} + 5\,F_{i,j} + 2\,F_{i+1,j}\right)}{6}$$

$$S_2 = \frac{\left(2\,F_{i,j} + 5\,F_{i+1,j} - F_{i+2,j}\right)}{6}$$

WENO method use a weighted average of the stencils to obtain the numerical value of the parameters in a cell. With this propose, the method set a comparation of a hierarchy of undivided differences, which can be used to measure the smoothness of the numerical flux. The interpolation stencil is defined as a function of S_k. For $r = 3$ these interpolations are:

$$IS_0 = \frac{13}{12}\left(F_{i-2,j} - 2\,F_{i-1,j} + F_{i,j}\right)^2 + \frac{1}{4}\left(F_{i-2,j} - 4F_{i-1,j} + 3F_{i,j}\right)^2$$

$$IS_1 = \frac{13}{12}\left(F_{i-1,j} - 2\,F_{i,j} + F_{i+1,j}\right)^2 + \frac{1}{4}\left(F_{i-1,j} - F_{i+1,j}\right)^2$$

$$IS_2 = \frac{13}{12}\left(F_{i,j} - 2\,F_{i+1,j} + F_{i+2,j}\right)^2 + \frac{1}{4}\left(3\,F_{i,j} - 4\,F_{i+1,j} + F_{i+2,j}\right)^2$$

The weight of each function in Eq. 2.28 are shown in Eq. 2.30.

$$\psi_0 = \frac{1/10}{(\epsilon + IS_0)^3}$$

$$\psi_1 = \frac{6/10}{(\epsilon + IS_1)^3}$$

$$\psi_2 = \frac{3/10}{(\epsilon + IS_2)^3}$$

$$\psi_{total} = \psi_0 + \psi_1 + \psi_2$$

Eq. 2.30

Where $\epsilon = 10^{-6}$. Therefore:

$$\omega_k = \frac{\psi_k}{\psi_{total}}$$

Eq. 2.31

Finally, the numerical flux at the interface is the weighted average presented in Eq. 2.32.

$$\tilde{F}^+_{i+\frac{1}{2},j} = \omega_0\, S_0 + \omega_1\, S_1 + \omega_2\, S_2$$

Eq. 2.32

Repeating the process for $\tilde{F}^-_{i+\frac{1}{2},j}$, $\tilde{F}^+_{i-\frac{1}{2},j}$ and $\tilde{F}^-_{i-\frac{1}{2},j}$ the numerical flux can be obtained as:

$$\tilde{F}_x = \frac{1}{\Delta x}\left(\left(\tilde{F}^+_{i+\frac{1}{2},j} + \tilde{F}^-_{i+\frac{1}{2},j}\right) - \left(\tilde{F}^+_{i-\frac{1}{2},j} + \tilde{F}^-_{i-\frac{1}{2},j}\right)\right)$$

Eq. 2.33

2.1.3.4.   Boundary condition

The computational domain for an underexpanded jet is schematically represented in Figure 2.6. The size of the domain covers $31D \, x \, 5D$, extending $30D$ from the nozzle exit and $5D$ from the jet centerline (D is the diameter of the nozzle exit). It has been assumed that at these distances the jet does not have any influence in the domain. The primitive variables (ρ, u, v, p) must be defined in all the boundaries of the domain ($B1, B2, B3, B4, B5 \ and \ B6$) since they are involved in the flux vector. As it can be observed in Figure 2.6, only half of the nozzle is simulated to reduce the mesh size in a half and the calculation time. The condition imposed in the boundaries are:

- B1: nozzle exit condition.
- B2 (wall of nozzle): non-reflecting boundary condition.
- B3: atmosphere conditions.
- B4: atmosphere conditions.
- B5 (centerline): symmetric condition with $v = 0$.
- B6: atmosphere conditions.
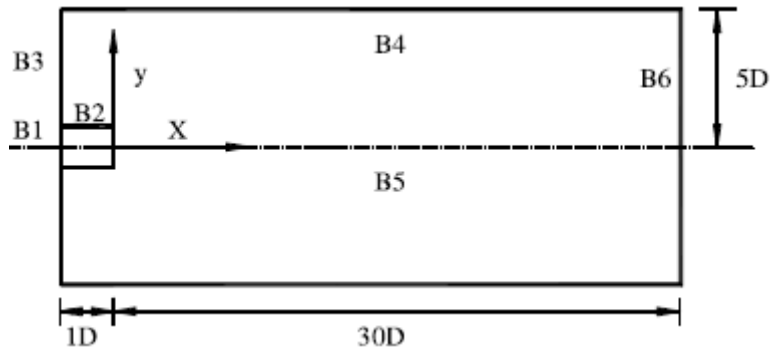
Figure 2.6. Schematic diagram of the computational domain for supersonic jet (Cheng & Lee, 2005).

Four set of uniform mesh ($310\ x\ 10, 500\ x\ 110, 625\ x\ 140\ and\ 730\ x\ 160$) have been analyzed by (Cheng & Lee, 2005) for the mesh independence study. The solution for the meshes $625\ x\ 140\ and\ 730\ x\ 160$ is the same. Therefore, the mesh independence is reached for the mesh $625\ x\ 140$ and this is the mesh size used in the jet simulations.

All statistical data presented for supersonic jet are obtained by averaging over an appropriate period of time ($100 \le t/(D/u_e) \le 125$).

2.2.   Schlieren Systems

2.2.1.   Digital image basic concepts

An image may be defined as a two-dimensional function, $f(x, y)$, where x and y are spatial (plane) coordinates, and the amplitude of f at any pair of coordinates (x, y) is called the intensity or gray level of the image at that point (Gonzalez & Woods, 2008). When x, y, and the intensity values of f are all finite, discrete quantities, we call the image a digital image. The field of digital image processing refers to processing digital images by means of a digital computer. Note that a digital image is composed of a finite number of elements, each of which has a particular location and value. These elements are called pixels.

Images can be divided in two different groups regarding the information which is saved inside a pixel. An image can be chromatic or monochromatic. In a chromatic image (color) the basic components are red, green and blue (RGB), as the light seen by the eye, by film and by the photo sensor in a digital camera. The others color can be expressed as a function of the three-main color, varying its values between 0-255.

$$color = g(red, green, blue)$$

Eq. 2.34

Applying Eq. 2.34:

$$green = g(0,255,0); yellow = g(255,255,0); white = g(255,255,255); black = g(0,0,0)$$

Eq. 2.35

From the solution in Eq. 2.35, if all the RGB values reach their maximum the color obtained is white, whereas if all values are 0 the color obtained is black. Therefore, a gray scale is defined when the values of RGB are the same ($red = green = blue$). This colorless light is called monochromatic light. The main characteristic of the monochromatic light is its intensity or brightness. Because the intensity of monochromatic light is perceived to vary from black to grays and finally to white, the term gray level is used commonly to denote monochromatic intensity.

The range of measured values of monochromatic light from black to white is usually called the gray scale and the brightness can change from 0 to 255.

$$gray\ level = g(brightness)$$

Eq. 2.36

If the brightness is 0 the color obtained is black, whilst if it is 255 white is obtained. All intermediate values represent a gray amount in between black and white.

Another interesting concept related with digital image:

- Spatial resolution: measure of the smallest discernible detail in an image. Quantitatively, spatial resolution can be stated as pixels per unit. In the U.S.A., this measure usually is expressed as dots per inch (dpi). To give you an idea of quality, newspapers are printed with a resolution of 75 dpi, magazines at 133 dpi and glossy brochures at 175 dpi (Gonzalez & Woods, 2008).
  Photographic quality requires that print resolution should be not less than 300 dpi. In the present project, a resolution of 600 dpi is being used in the image processing system (25.4 mm / 0.04 mm/pixel = 600 dpi (ppi³)).
- Intensity resolution: refers to the smallest discernible change in intensity level. Based on hardware considerations, the number of intensity levels usually is an integer power of two. The most common number is 8 bits, with 16 bits being used in some applications in which enhancement of specific intensity ranges is necessary. Unlike spatial resolution, which must be based on a per unit of distance basis to be meaningful, it is common practice to refer to the number of bits used to quantize intensity as the intensity resolution. For example, it is common to say that an image whose intensity is quantized into 256 levels has 8 bits of intensity resolution.

2.2.2. Refractive Behavior of Fluids

2.2.2.1. Relation between Fluid Density and Refractive Index

The refractive index (n) can be defined as how much the path of the light is bent when it changes the medium in which spread. The index can be defined as:

$$n = \frac{c}{v}$$

Eq. 2.37

Where c is the speed of the light in vacuum and v is the velocity of the light in the medium. It is a dimensionless number. For the following study, it is necessary to obtain a relationship between the density of the medium and its refractive index. The equation Gladstone-Dale (Eq. 2.38) is an empirical equation which relates refractive index and density as follow:

$$n - 1 = K_{GD}\ \rho$$

Eq. 2.38

Where n is the refractive index, K_{GD} the Gladstone-Dale constant $[m^3/kg]$ and ρ the density. Taking derivatives over the displacement, the variation of the refractive index can be calculated as:

$$\frac{\partial n}{\partial x} = K_{GD} \frac{\partial \rho}{\partial x}$$

Eq. 2.39

2.2.2.2. Angle of refraction

The variation of the trajectory of the light ray is an important parameter in order to obtain quantitative information using Schlieren System. Figure 2.7 shows a scheme of a light ray moving from a medium with a refractive index n to a different medium with a refraction idex of $n + \Delta n$. The incidence angle θ change to a new incidence angle $\theta + \Delta \theta$. Therefore, the angle of refraction can be defined as $\Delta \theta$ and can be calculates using the Snell's law (Eq. 2.40) as follows.

$$\frac{n + \Delta n}{n} = \frac{\sin(\theta)}{\sin(\theta + \Delta\theta)}$$

Eq. 2.40

From the trigonometric addition formula of the sine $(\sin(\alpha + \beta) = \sin(\alpha)\cos(\beta) + \cos(\alpha)\sin(\beta))$ and assuming $\Delta\theta$ is very small $(\cos(\Delta\theta) \simeq 1 \ and \ \sin(\Delta\theta) \simeq \Delta\theta)$,

$$1 + \frac{\Delta n}{n} = \frac{1}{1 + \Delta\theta \dfrac{\cos(\Delta\theta)}{\sin(\Delta\theta)}}$$

Eq. 2.41

Therefore, developing Eq. 2.41:

$$1 + \frac{\Delta\theta\cos(\Delta\theta)}{\sin(\Delta\theta)} + \frac{\Delta n}{n} + \frac{\Delta n}{n}\frac{\Delta\theta\cos(\Delta\theta)}{\sin(\Delta\theta)} = 1$$

Eq. 2.42
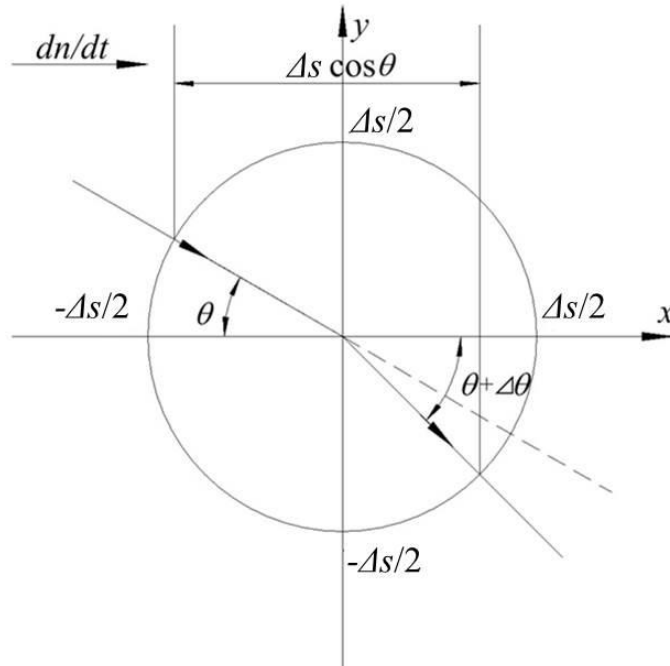
Figure 2.7. Schematic diagram of refraction of light beam.

For small values of $\Delta\theta$ and Δn, the last term in the left-hand of the Eq. 2.42 is approximated zero. Therefore:

$$\Delta\theta = -\frac{\sin(\theta)}{\cos(\theta)}\frac{\Delta n}{n}$$

Eq. 2.43

From Figure 2.7, and assuming small variation of θ, it is straightforward to derive the following equations:

$$\frac{\Delta n}{\Delta x} = \frac{dn}{dx}$$

Eq. 2.44

$$\Delta x = \Delta s \cos(\theta)$$

Eq. 2.45

$$\Delta n = \frac{dn}{dx}\Delta n \cos(\theta)$$

Eq. 2.46

Combining Eq. 2.43 with Eq. 2.46 the angle variation can be found as a function of the path variation (Δs), the refractive index (n) and its variation over x, and the incidence angle.

$$\Delta\theta = -\frac{1}{n}\left(\frac{dx}{dn}\right)\Delta s \sin(\theta)$$

Eq. 2.47

However, the refractive index is not constant along a medium. The general solution can be expressed as an integration as following:

$$\Delta\theta = \int \frac{1}{n}\left(\frac{\partial n}{\partial x}\right)ds$$

Eq. 2.48

Assuming $n \simeq 1$ for air and combining Eq. 2.48 with Eq. 2.39 the variation of the angle can be expressed as function of the variation of density.

$$\Delta\theta = \int \left(\frac{\partial\rho}{\partial x}\right)ds$$

Eq. 2.49

Eq. 2.49 will be used in Section 2.2.4 to obtain quantitative values of the Schlieren methods. This equation will allow to relate the brightness obtained in the experiments with the density variation of the target.

2.2.3. Basic principles

Schlieren systems are used to measure the amount of light deflection generated by a transparent optical phase object. In the fundamental arrangement, mostly referred to as the *Toepler system* (Marton & Marton, 1981), a parallel light beam traverses the test object and is focused thereafter by means of lens named *Schlieren Lens*. An image of the light source is formed

in the focal point of the Schlieren lens. A knife-edge is placed in the plane of the light source image to cut off part of the transmitted light. The light beams which cross the targets might be deflected, changing their path and their focal point. The camera placed after the focusing lens receive a reduced intensity of light due to the knife located at the focal point. Figure 2.8 shows a target of a Schlieren experiment and a simplified scheme. The dashed lines represent the deflected beam. As we can see, one of the beam is blocked by the knife; therefore, the light intensity which reach the camera is reduced.
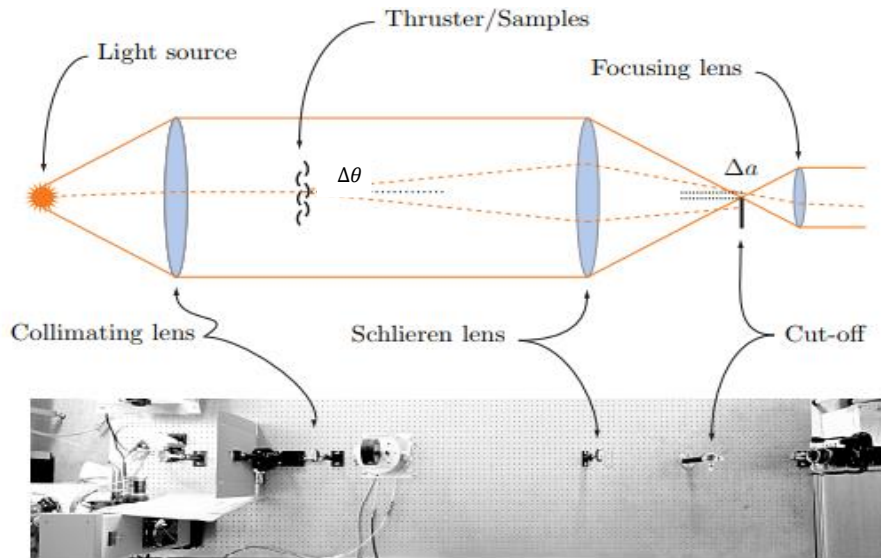
Figure 2.8. Schlieren setup in simplified schematic (top) with Δθ denoting the angle of refraction of a light ray and Δa the resulting displacement at the cut-off. Bird's eye view of the actual setup (bottom), from left to right: light source, lens, variable slit, collimating lens, test object, Schlieren lens, cut-off and camera (Lekholm, 2012).

The key element of the Schlieren method is the knife mentioned above. The deflected light is blocked by the knife edge and the screen is darkened. Therefore, the knife serves as a cut-off filter of intensity. The term that quantify the phenomenon is called *contrast,* which can be obtained as the ratio between the variance of the brightness (ΔB) over the measured of the brightness without knife (B_n). The change in the *contrast* depends on the initial intensity distribution on the screen.

$$contrast = \frac{\Delta B}{B_n}$$

Eq. 2.50

The direction of the knife edge provokes differences in the density gradients recorded. The light blocked is not recorded by the camera, so this part is darkened. Observing the recorded Schlieren image, it discriminates relative changes rather than absolute values.

2.2.4. Quantitative Schlieren system

Once the basic concepts of Schlieren system has been introduced, it will be evaluated quantitatively. In Figure 2.9, the image of the light source is a small square and only certain height (Δa) is allowed to pass over the knife. The knife edge is located at the focal distance (f_s) of the Schlieren lens. With a homogeneous test field, the recording plane is evenly illuminated with an intensity or brightness (B_n) equal to constant, which is dependent of the height a and the focal distance f_f of the focusing lens.

$$B_n = \frac{a_n}{a_0} B_0$$

Where B_0 is the illumination when no know is presented in the system. Eq. 2.51 is held only if geometrical aberration of the optical system, e.g., coma and astigmatism, can be neglected.
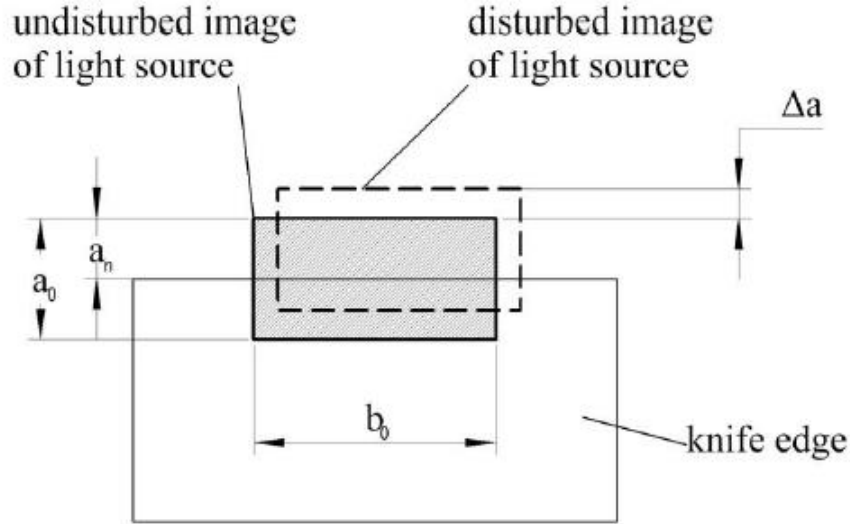
Figure 2.9. Image of the light source in the plane of the knife edge (Nazari A. , 2017).

Light rays deflected by an angle $\Delta\theta$ due to a disturbance in the test field cause a vertical shift of the light source image by an amount Δa (Figure 2.8).

$$\Delta a = f_s \tan(\Delta\theta) \simeq f_s \Delta\theta$$

Where f_s is the focal length of the Schlieren length. The light intensity is modified by the same factor as Eq. 2.15.

$$\Delta B = B - B_n$$

ΔB can be defined as the brightness deviation on the Schlieren screen, using as reference the brightness (B_n) when there is not disturbance in the medium. Therefore, with Eq. 2.49, Eq. 2.51 and Eq. 2.53, the relative brightness change produced by the disturbed test object in a point of the recording plane is given by:

$$contrast = \frac{\Delta B}{B_n} = \frac{\Delta a}{a} = \Delta\theta \frac{f_s}{a}$$

And from the respective optical analysis (Eq. 2.49), which relates the deflection angle to the refractive index variation in the test field, it follows that:

$$\frac{\Delta B}{B_n} = \frac{f_s}{a} K_{GD} \int \left(\frac{\partial \rho}{\partial x}\right) ds$$

<div align="center">Eq. 2.55</div>

If the knife is rotated 90º, the deflection angle on y-axis will be measured, then,

$$\frac{\Delta B}{B_n} = \frac{f_s}{a} K_{GD} \int \left(\frac{\partial \rho}{\partial y}\right) ds$$

<div align="center">Eq. 2.56</div>

Eq. 2.56 shows that the Schlieren photograph taking with the Toepler system exhibit changes in the relative brightness which can be represented as variation of the refractive index or density gradient in the normal direction to the knife edge.

2.3. 3D-CT method

3D-CT (Three-dimensional computer tomography) method makes use of measurement of a target taking from different direction (θ_i) to obtain different cross-section of it and create a 3D volume representation. 3D-CT process requires 2D distributions (images) of the deviation density thickness ($Dt(\theta)$) called "projection", which is defined by the line-of-sight- integration of density deviation from ambient gas density, to obtain deviation density distribution ($\Delta\rho(x, y)$) in each point of the cross-sections. The calculation of $Dt(\theta)$ based on brightness of photographs is fully development in section 3.3.

The reconstructed $\Delta\rho(x, y)$ is converted in 2D density distribution $\rho(x, y)$ as follows.

$$\rho(x, y) = \Delta\rho(x, y) + \rho_a^*$$

<div align="center">Eq. 2.57</div>

The 2D distribution $\rho(x, y)$ is accumulated in layers to form 3D-CT distribution $\rho(x, y, z)$.

The CT is performed in 2 steps:

- Data acquisition: deviation density thickness values obtained using 20-directional quantitative Schlieren photography (Section 3)
- Image reconstruction from projection ($Dt(\theta)$): in this study, a method named Distributed Back Projection (DBP) is used an image reconstruction. This method uses an algorithm based on a simpler processing method called Maximum Likelihood-Expectation Maximization (ML-EM).

2.3.1. ML-EM method

ML-EM method is the combination of two different method.

- Maximum likelihood method (ML): is a method of estimating the parameters of a statistical model, given observations.
- Expectation maximization method (EM): is an iterative method to find maximum likelihood or maximum a posteriori (MAP) estimates of parameters in statistical models, where the model depends on unobserved latent variables.

Firstly, we introduce the ML method. We assume a discrete cross-section of m pixels, each of them has a reconstructed value (λ_j) which is the brightness of the corresponded pixel. Let be x the real brightness measured by the camera and C the measurement probability. The probability

makes reference to the likelihood of the measuring instrument to be reached by the photon emitted by the pixel.

Assuming that the number of measurement is n, the ML of λ_j is expressed as

$$\lambda_j = \frac{\sum_{i=1}^{n} x_i}{\sum_{i=1}^{n} C_i}$$

Eq. 2.58

Nevertheless, brightness in one pixel cannot be isolated from the surround pixels. Therefore, the value measured by the camera is the brightness of all the peripheral pixels. In Figure 2.10, it is shown a model of ML-EM to calculate the brightness of the pixel of a cross-section, knowing the brightness measured of the different device (y_{ij}). i refers to the device which has made the measurement and j is the detector or pixel in the detector group.
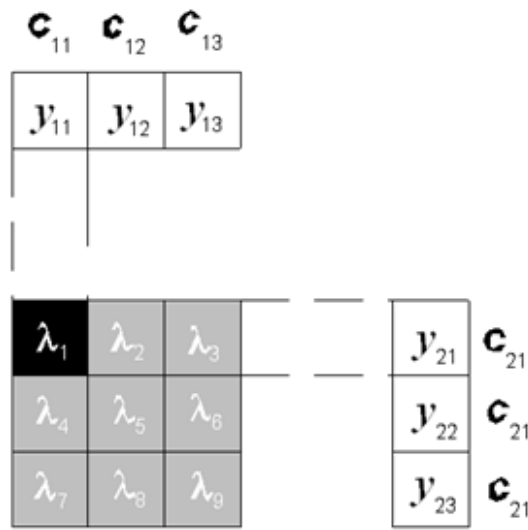
Figure 2.10. EM estimation (Nazari A. , 2017).

y_{ij} is defined as the summation of all the λ_j in the same direction over the probability C_{ij}. For example:

$$y_{11} = \frac{\lambda_1 + \lambda_4 + \lambda_7}{C_{11}}$$

$$y_{23} = \frac{\lambda_7 + \lambda_8 + \lambda_9}{C_{21}}$$

Eq. 2.59

In this way, x_{ij} is set as the brightness value detected by the j detector (pixel) of the group i only by λ_j. x_{ij} can be expressed as:

$$x_{ij} = \frac{y_{ij} \, C_{ij} \, \lambda_j}{\sum_{j=1}^{n} C_{ij} \, \lambda_j}$$

Eq. 2.60

Therefore, the numerical value (λ) of the pixels can be obtained using Eq. 2.61 which is a combination of Eq. 2.58 and Eq. 2.60 (Ishino, et al., 2015).

$$\lambda_j = \frac{\lambda_j}{\sum_{j=1}^{n} C_{ij}} \sum_{i=1}^{m} \frac{y_{ij} \, C_{ij}}{\sum_{j=1}^{n} C_{ij} \, \lambda_j}$$

<div align="center">Eq. 2.61</div>

As λ_j is in both side of Eq. 2.61, an iterative method is required to solve the equation, since it is impossible to solve analytically. The EM is the method used to solve it (Eq. 2.62):

$$\lambda_j^{k+1} = \frac{\lambda_j^k}{\sum_{j=1}^{n} C_{ij}} \sum_{i=1}^{m} \frac{y_{ij} \, C_{ij}}{\sum_{j=1}^{n} C_{ij} \, \lambda_j^k}$$

<div align="center">Eq. 2.62</div>

Where k is the iteration number. The algorithm converges to the maximum likelihood estimate of a probability distribution function from the observed data. All projection data (y_{ij}) are distributed along the projection beam at the back-projection progress. It is, therefore, recommended that this CT method should be referred to as Distributed Back-Projection (DBP) method.

3. Experimental method (20-directional quantitative Schlieren photography)

The concept of 20-directional quantitative Schlieren photography is represented in the Figure 3.1 which was created using the concept explained in Section 2.2 of a single quantitative Schlieren photography.
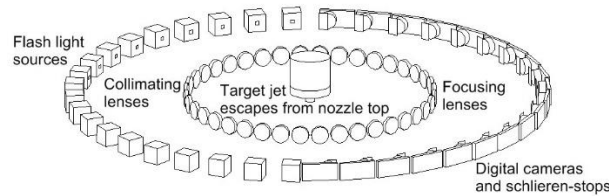
Figure 3.1. 20-directional Schlieren photography scheme (Ishino, et al., 2016).

The single unit is composed of two achromatic lenses of 50 mm in diameter and 300 mm in focal length, a light source unit, a vertical knife edge or Schlieren stop, and a digital camera. The Schlieren system is located in a place where the ambient density can be considered as $\rho_a^* = 1.2 \; kg/m^3$.
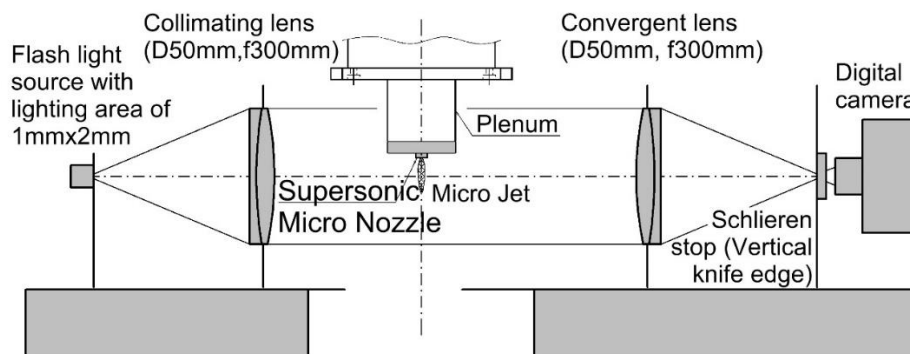
Figure 3.2. Single unit of quantitative Schlieren optical system of the multi-directional Schlieren camera (Nazari A. Z., et al., 2017).

Figure 3.3 shows the custom-made 20-directional Schlieren camera, which consist of 20-single system. The 20-single system are equispaced 9º starting from $\theta_1 = -85.5º$ and finishing in $\theta_{20} = 85.5º$. The angle θ_i represents the camera direction and is defined as the horizontal angle from x-axis. In this study, the horizontal configuration is used.
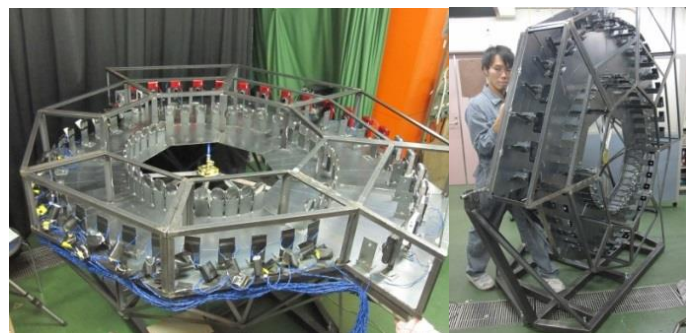
Figure 3.3. The 20-directional Schlieren camera. The horizontal position is shown on the left and the vertical position on the right (Ishino, et al., 2016).

The xyz-coordinated system of the 20-directional Schlieren system has its origin in the micro-nozzle exit. As shown in Figure 3.4, the z-axis is set normal to the nozzle exit and the x-axis is located between camera 10 ($\theta_{10} = -4.5^\circ$) and 11 ($\theta_{11} = 4.5^\circ$).
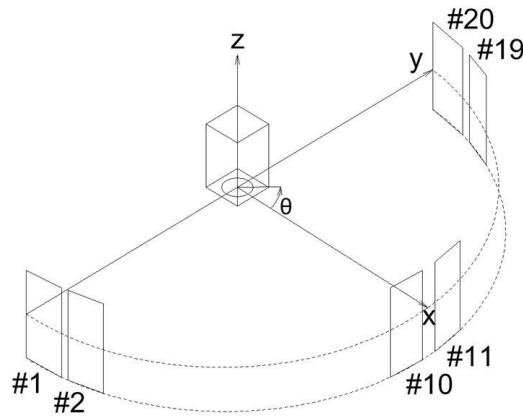
Figure 3.4. Coordinated system of 20-directional Schlieren photography (Nazari A. , 2017).

3.1. Apparatus

In this section, the specifications of the different devices used in the multi-directional quantitative Schlieren system are explained. From points 1-7, the devices correspond to the Schlieren system; and points 8 and 9 are related with the target.

1. Flashlight

The light unit is the element which illuminate the target. It has to provide a uniform luminance. The intensity of the light as well as the shape of the unit must be defined and are vital for the successful of the experiment. Ahead of the light unit, a slit is attached to control the size and the lightning area. The specification of the light unit used in the 20-directional quantitative Schlieren system are the following:

- Type: xenon flash lamp.
- Condenser capacity: 3.3 μF.
- Luminance time: 35 μs.
- Charging time: 30 s.
- Light source size (slit): 1x2 mm (width x height).
- Light source shape (slit): rectangle.

The luminance time is short enough to measure un-steady phenomenon such us turbulent flames or transition flow (not fully developed).

The emission time and intensity must be the same for each camera of the system. For it, the light emission is made with a constant charging time, as well as the battery should have sufficient charge which use in switchbox. Accordingly, the procedure of 20-directional quantitative Schlieren photography is briefly shown:

1. Discharge the flash lamp and wait 30 seconds.
2. Perform the measurement.

2. The first and second lens

Both, Collimating lens and Convergent lens (Schlieren lens) have the same characteristics. Their specifications are:

- Type: Plano convex achromatic lens.
- Focal length: 300 mm.
- Lens diameter: 50 mm.

3. The Schlieren stop

The purpose of this device is to stop the deflected rays which do not pass through the focal point. This Schlieren stop is also called knife. In the Schlieren system of the present study the knife is located from left to right. As it has been mentioned before, the orientation of the knife edge has influence in the directional density gradient.

- Type: Simple razor blade.
- Orientation: Vertical from left to right.
- Light blocking width: 0.5 mm.

4. Digital camera

The camera used in the Schlieren system of the present study is a commercial digital mirrorless model with a modification in its lens. Figure 3.5 shows the commercial model on the left and the modified on the right. The original lenses are removed and substituted with those shown in Figure 3.6. Also, the light quantity is adjusted by using stepped ND filter[5]. The camera specifications are:

- Model: NIKON 1 J1.
- Focal length: 30 mm.
- Image sensor type: CMOS.
- Shutter speed: 33 ms.

Figure 3.5. Digital mirrorless single-eye camera (modified camera (left), commercial camera (right)).

5. 5 groups – 6 lenses

Figure 3.6 shows the 5 groups – 6 lenses that are attached to the camera in Figure 3.5. The lens specifications are shown below.

---

[5] In photography and optics, a stepped neutral-density filter, or stepped ND filter, is a filter where density and transmission vary in equal steps across the surface length. The steps are abrupt changes and no white light escapes between them. Spectrally flat neutral density coating. Ideal for applications requiring variable densities and known density values.

- Lens composition: 5 groups – 6 sheets.
- Focal length: 30 mm.
- Front diameter: 10 mm.
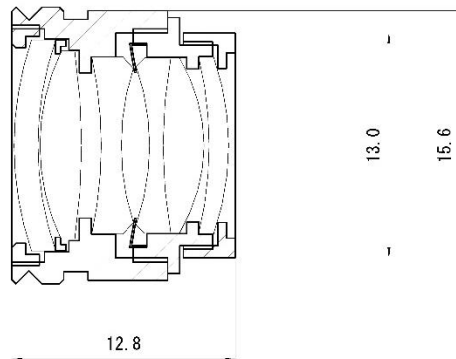
Figure 3.6. Camera lens outline (Nazari A. , 2017).

6. Corresponding circuit

Figure 3.7 shows the synchronous circuit of flash light and camera implemented in the 20-directional quantitative Schlieren system. Its main propose is to adjust the flash light and camera timing to do the 20 measurements simultaneously.
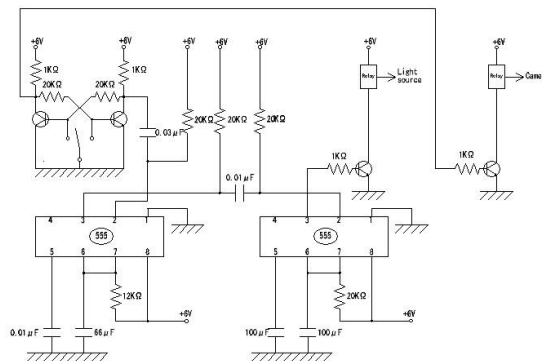
Figure 3.7. Synchronous circuit (Nazari A. , 2017).

7. High-speed camera

For pre-investigation work and also for time analysis there is an extra camera installed in the Schlieren system which can work simultaneously with the others cameras of the system. This high-speed digital camera can capture high resolution images, as well as record movies. Moreover, this camera has the option of slow motion playback. The specifications of the high-speed camera are shown below.

- Model: Photron made FASTCAM-512 PCI 2K.
- Frame rate at full pixel resolution: 2000 frames per second (fps).
- Frame rate at reduced pixel resolution: 32000 frames per second (fps).
- Image sensor type: CMOS.
- Shutter speed: 16.7 ms to 4 μs.
- Full element resolution: 512x512 Pixel.
- Monochrome tone density: 10-bits (1024 steps).
- Color tone density: 32-bits.

The Schlieren system used for the high-speed camera is display in Figure 3.8. It has the typical devices used by a Schlieren system (2 achromatic lenses, a continuous light source and a Schlieren stop). The camera is installed with an elevation angle of 6.6º, and as it can be seen in Figure 3.9, it is placed between cameras number 13 and 14 with a direction of 27º. For photographing, a Nikon single-lens reflex (focal length 50 mm, F value 1.4) is attached to the high-speed camera, and a white LED pinhole type light source with a diameter of 0.75 mm is used.
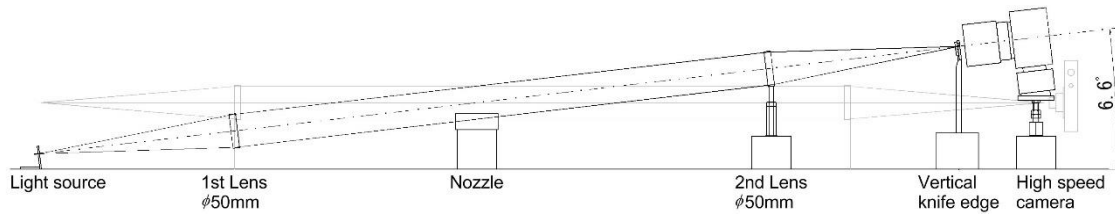
Figure 3.8. Schematic diagram of high-speed Schlieren optical system (Nazari A. , 2017).
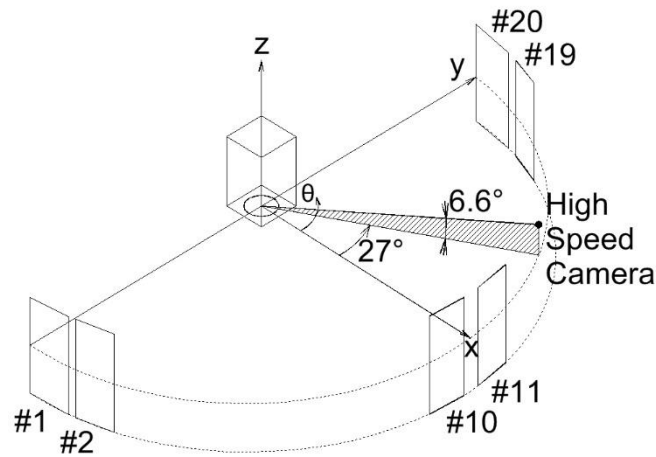
Figure 3.9. High-speed camera installation position (Nazari A. , 2017).

8. Convergent-Divergent (Laval) micro nozzles

The Figure 3.10 shows the general nozzle used in the present study. Its characteristics are shown in detail ahead.

Figure 3.10. Micro nozzle (Fukuda, et al., 2016).

This circular axisymmetric convergent-divergent nozzle is designed to work at a Mach number of $M_d = 1.5$. Its main geometrical features are the throat diameter of 922 μm, the exit diameter of 1000 μm and the expansion area ratio of 1.18. Further details are illustrated in Figure 3.11. The center of the micro nozzle exit has been selected as origin of xyz-coordinated system.
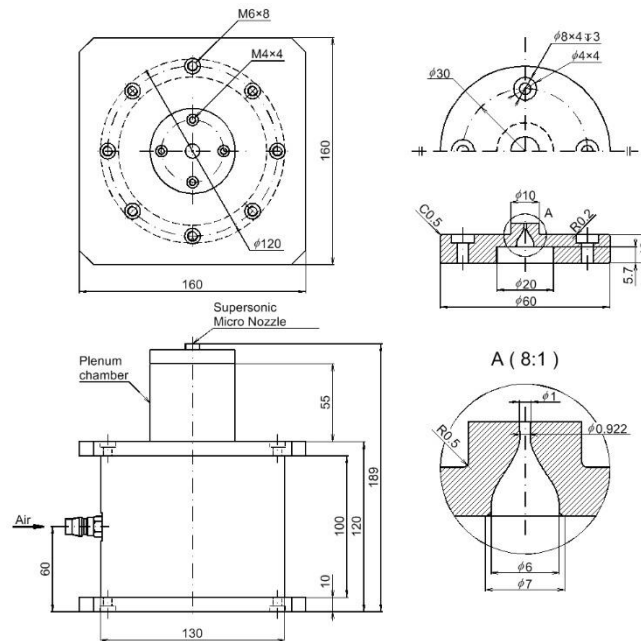
Figure 3.11. Circular micro nozzle (units: mm) (Fukuda, et al., 2016).

Figure 3.12 shows the functions which control the design of the micro nozzle walls. Until the throat (A-B), the wall shape is controlled by the function represented Figure 3.12. From the throat (B-C) the wall contour is designed using the axisymmetric method of characteristic[6] to provide uniform and parallel flow at the downstream of the micro nozzle exit (Foelsch, 1949).
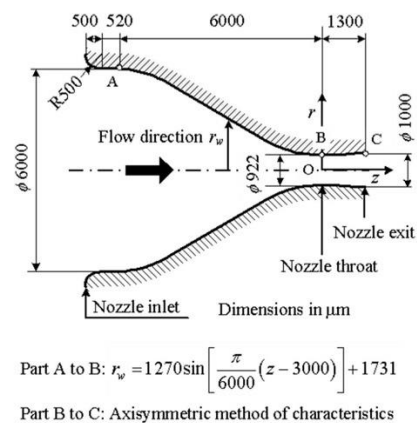
Figure 3.12. Internal detail of circular micro nozzle (units: μm) (Fukuda, et al., 2016).

---

[6] The method of characteristics is a technique for solving partial differential equations. Further information can be found in (Foelsch, 1949).

9. Air supply system

The nozzle is supplied with air by an air delivery system. A pressure gauge and a flowmeter from SMC Co. are used as measuring instrument. A scheme of the air supply system is represented in Figure 3.13.
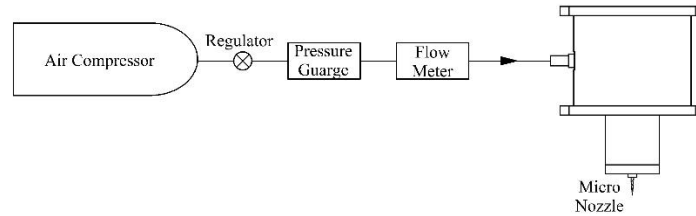
Figure 3.13. Air supply system scheme (Nazari A. , 2017).

The specifications of the air supply components of Figure 3.13 are shown below.

- Pressure gauge specification:
  - Model: SMC ISE30A.
  - Rated pressure range: -0.1 to 1.0 MPa.
  - Withstand pressure: 1.5 MPa.
  - Display/Minimum unit setting: 0.001 MPa.
  - Power supply voltage: 12 to 24 VDC ± 10%
  - Operating temperature range: Operating: 0 to 50 ºC, Stored: -10 to 60 ºC (no freezing or condensation).
- Flow meter specifications:
  - Model: SMC PFM750.
  - Flow rate range: 1 to 50 L/min.
  - Rated pressure range: -70 to 750 kPa.
  - Minimum unit setting: 0.1 L/min.
  - Power supply voltage: 24 VDC ± 10%.
  - Operating fluid temperature: 0 to 20 ºC (with no freezing and condensation)
- Air compressor specifications:
  - Model: PAOCK UD-1010 II.
  - Maximum working pressure: 0.8 MPa.
  - Tank capacity: 10 L.
  - Flow rate: 90 L/min.

3.2.   Flow condition

The present study is tasting a supersonic micro nozzle with circular cross-section working at underexpanded condition. This means that the working condition must meet a jet pressure ratio (JPR) bigger than one or the exit Mach number greater than the design Mach number:

$$P_e/P_b > 1.0 \; ; \;\; M_j > M_d$$

Eq. 3.1

In order to meet this condition, the nozzle pressure ratio (NPR) imposed in the nozzle must be beyond the design condition, $DNPR = 3.67$. Flow condition for underexpanded supersonic micro-jets are summarized in Table 3.1 and Table 3.2.

Ambient Temperature	T_b	300.35 K (27.2 ºC)
Back (ambient) pressure	P_b	0.101 MPa
Nozzle design Mach number	M_d	1.5
Nozzle exist diameter	D	1000 μm (1 mm)

Table 3.1. Ambient and micro nozzle condition (circular nozzle).

Nozzle pressure ratio (NPR)	P_0/P_b	4.0	4.5	5.0
Absolute (Stagnation) pressure	P_0	0.404 MPa	0.455 MPa	0.505 MPa
Gauge pressure	P_G	0.303 MPa	0.354 MPa	0.404 MPa
Jet pressure ratio (JPR)	P_e/P_b	1.090	1.226	1.362
Exit pressure	P_e	0.110 MPa	0.124 MPa	0.138 MPa
Fully expanded jet Mach number	M_j	1.559	1.638	1.709
Fully expanded jet density	ρ_j	1.74 kg/m^3	1.80 kg/m^3	1.86 kg/m^3
Fully expanded jet diameter	D_j	1018 μm	1044 μm	1070 μm

Table 3.2. Underexpanded supersonic micro-jets flow conditions (circular nozzle).

3.3. Measurements

In this section we are going to introduce the different pictures which must be taken in order to obtain an accurate 3D-CT reconstruction of the supersonic jet. All pictures are transformed from *.jpg* extension to *.pgm*, since we want to work with gray scale.

The first objective is to set the same reference system for all the pictures, since they will be used simultaneously in CT-reconstruction. A circular cross-section rod is placed in the working environment (Figure 3.14 (left)), so a reference system can be set for each camera taking as reference the rod. Pictures are rotated so the rod is perfectly vertical and are trimmed, deleting useless data ((Figure 3.14 (right)).
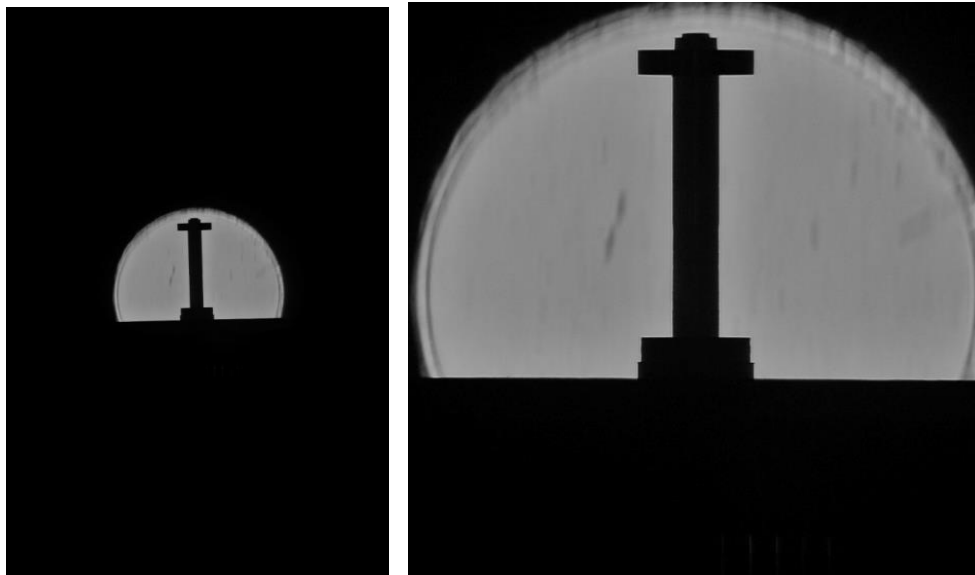
Figure 3.14. Rod picture (camera 11).

Figure 3.15 shows the working environment where the nozzle is placed (no-jet condition). This will set the reference value for the brightness, so the value of the contrast of the quantitative Schlieren system can be calculated (Section 2.2.4).
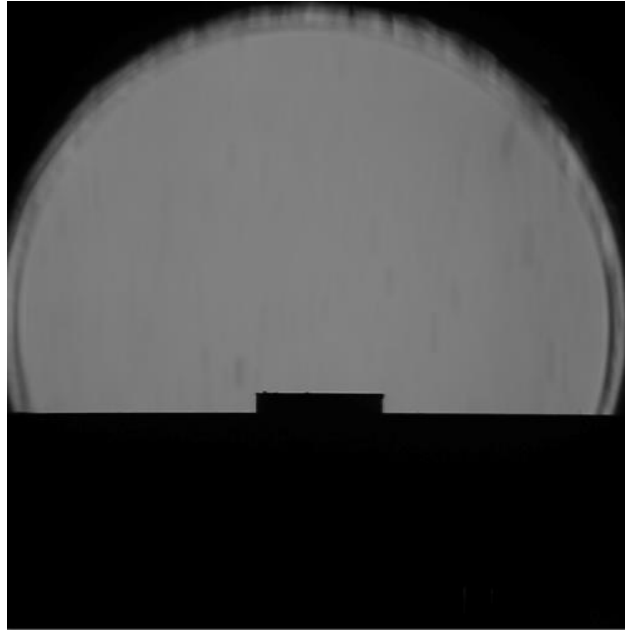
Figure 3.15. Working environment picture (camera 11).

Finally, the jet picture is done. In Figure 3.16 a sample of a jet operating at NPR 5 can be observed. Using Figure 3.15 and Figure 3.16 deviation density thickness can be calculated (Section 3.4)
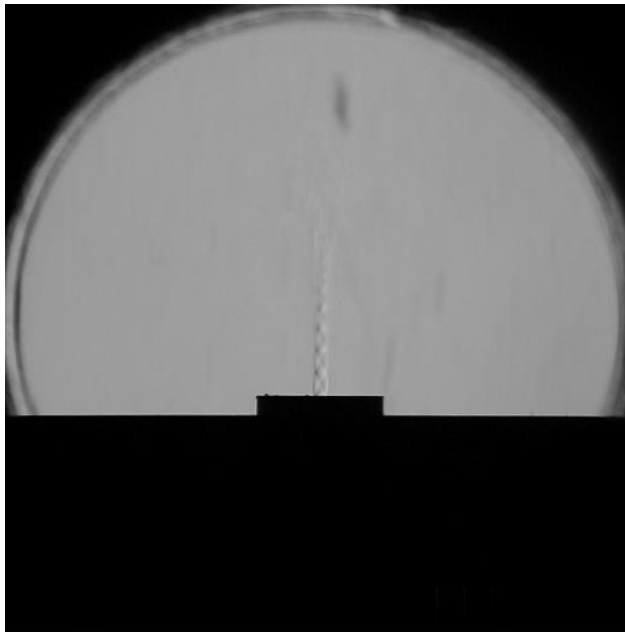
Figure 3.16. Supersonic jet picture working at NPR 5 (camera 11).

Additionally, a picture of a gray scale which is used to measure the range of brightness and to stablish the density range.
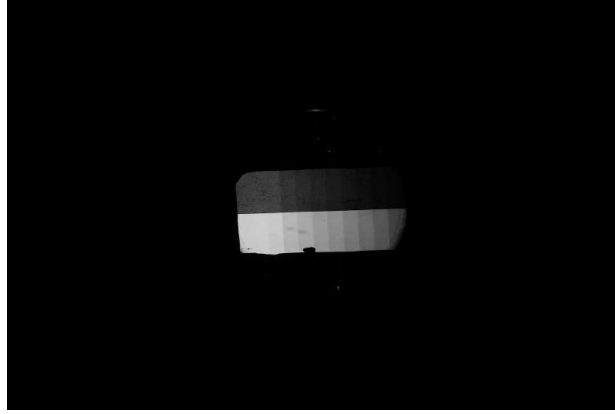
Figure 3.17. Gray scale (camera 11).

3.4. Deviation density thickness calculation

In Section 2.3 it was said that deviation density thickness ($Dt(X(\theta))$) is needed for CT-reconstruction. Deviation density thickness is called in CT-reconstruction "projection", which is defined by the line-of sight-integration of density deviation from ambient gas density (ρ_a^*). $Dt(X(\theta))$ is calculated for each direction of the 20-directional quantitative Schlieren system using the brightness of the images taken by the 20 cameras.

Figure 3.18 indicates the conversion process of image data. The used variables in Figure 3.18 are summarized in Table 3.3. Figure 3.18 (a) depicts density distribution $\rho^*(x,y)$ of target flow having an ambient gas (air) region of constant density ρ_a^* on a peripheral range of radius R.

f	The focal length of convergent lens (second lens)
K_{GD}	Gladstone-Dale constant for air ($K_{GD} = 2.2587 \cdot 10^{-4} \ m^3/kg$)
$B(X)$	Brightness of Schlieren image
$B_{nj}(X)$	Brightness of Schlieren image in no-jet condition (without any disturbance in the test section)
$\Delta B(X)$	Deviation brightness in Schlieren image
ρ	Density (kg/m^3); derived value, ($\rho = \Delta\rho + \rho_a^*$)
ρ^*	Density (kg/m^3); actual value
ρ_{ref}	Density of reference (kg/m^3)
ρ_a^*	Density of ambient air (kg/m^3); actual value
$\Delta\rho$	Deviation density (kg/m^3); derived value
$\Delta\rho^*$	Deviation density (kg/m^3); actual value, ($\Delta\rho^* = \rho^* - \rho_a^*$)
Dt	Density thickness of deviation density ($m \cdot kg/m^3$); derived value
Dt^*	Density thickness of deviation density ($m \cdot kg/m^3$); actual value
Dt'	Density thickness of deviation density plus thickness of Density thickness of deviation density ($m \cdot kg/m^3$); actual value ($m \cdot kg/m^3$)
Δs	Transparent width of light source image on Schlieren stop location

Table 3.3. Used expression in Figure 3.2.

Figure 3.18 (b)-(k) show observation in the direction of θ from x-axis. The inclined coordinated are denoted by $X(\theta)$ and $Y(\theta)$ as indicated in Figure 3.18 (a). For reference, Figure 3.18 (c) gives the deviation density in the line of Y (Eq. 3.2).
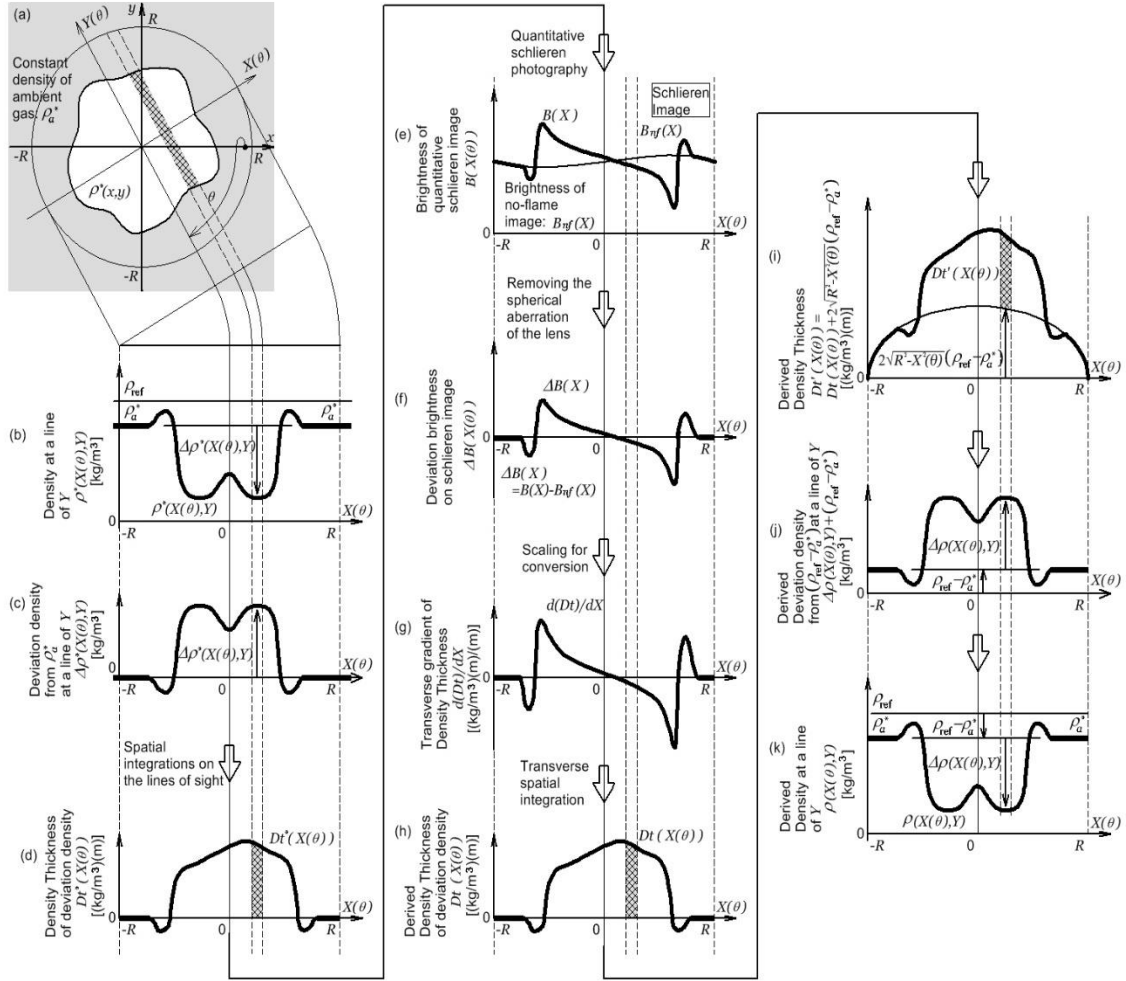
Figure 3.18. Processes of formation of Schlieren brightness and conversion to projections of Dt (Nazari A. Z., et al., 2017).

$$\Delta\rho^*(X(\theta),Y) = \rho_a^* - \rho^*(X(\theta),Y)$$

Eq. 3.2

$Dt^*(X(\theta))$ is obtained applying a spatially-integration of $\Delta\rho^*(X(\theta),Y)$ along the line of sight in Schlieren observation, given as a result Figure 3.18 (d). It can be observed that some values of $Dt^*(X(\theta))$ are smaller than 0. This is because there is some part of the target flow where the density is smaller than the ambient, which is used as reference.

Brightness of Schlieren image $B(X)$ (Figure 3.16) is given as x-directional gradient value of density thickness $Dt^*(X(\theta))$ shifted by brightness of Schlieren image in no-jet condition $B_{nj}(X)$ (Figure 3.15), indicated in Figure 3.18 (e).

Schlieren observation only present $B(X)$ and $B_{nj}(X)$. To obtain the density thickness $Dt(X(\theta))$ from $B(X)$ and $B_{nj}(X)$, both are processed in the following manners of Figure 3.18 (f)-(h). As indicated in Figure 3.18 (f), deviation brightness in Schlieren image $\Delta B(X)$ is given by Eq. 3.3 and results are shown in Figure 3.19 for each camera.

$$\Delta B(X) = B(X) - B_{nj}(X)$$

Eq. 3.3

33
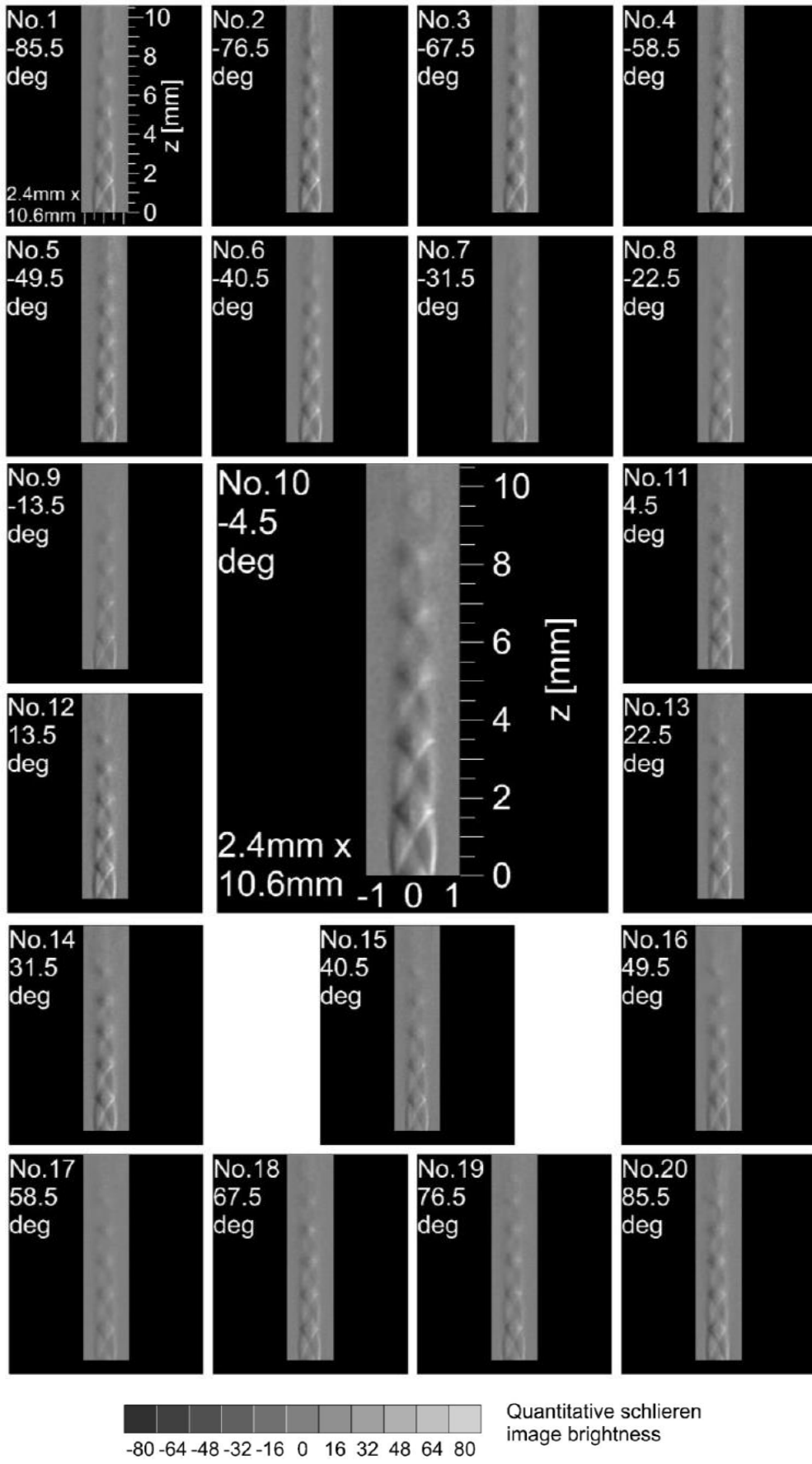
Figure 3.19. Deviation brightness in Schlieren image (Eq. 3.3) NPR 5 (Figure 3.18 (e)).

The number inserted in each image express the camera number and the shooting angle. Each image is 2.4mm x 10.6mm in size. A gray scale level showing the brightness value of quantitative Schlieren image is displayed below the image.

Eq. 3.3 is scaled to $d(Dt)/dX$ by Eq. 3.4. (Figure 3.18 (g)):

$$\frac{d(Dt)}{dX} = \frac{1}{K}\frac{\Delta s}{f}\frac{\Delta B(X)}{B_{nj}(X)}$$

Eq. 3.4

Derived density thickness of deviation density thickness ($Dt(X(\theta))$) is, therefore, reproduced by transverse-integration of $d(Dt)/dX$ from Schlieren images, as shown in Figure 3.18 (h). $Dt(X(\theta))$ can be expressed using Eq. 3.5. Images of $Dt(X(\theta))$ are presented in Figure 3.20.

$$Dt(X(\theta)) = \int_0^x \frac{1}{K}\frac{\Delta s}{f}\frac{\Delta B(X)}{B_{nj}(X)}dx$$

Eq. 3.5

Due to the presence of negative values that could appear in the CT-reconstruction $Dt(X(\theta))$ is shifted using Eq. 3.6 (Figure 3.18 (i)).

$$Dt'(X(\theta)) = Dt(X(\theta)) + 2\sqrt{R^2 - X^2(\theta)}\cdot(\rho_{ref} - \rho_a^*)$$

Eq. 3.6

The negative values of $Dt(X(\theta))$ during the CT-reconstruction are shifted to 0, since the code used in the CT-reconstruction cannot manage them. Therefore, with Eq. 3.6 this is avoided adding the thickness of $(\rho_{ref} - \rho_a^*)$ to $Dt(X(\theta))$.

Figure 3.21 shows the derived density thickness ($Dt'(X(\theta))$). Those are the data which are used in CT-reconstruction. The number inserted in each image express the camera number and the shooting angle. Each image is 2.4mm x 10.6mm in size. A gray scale level showing the deviation density thickness is displayed below the image.
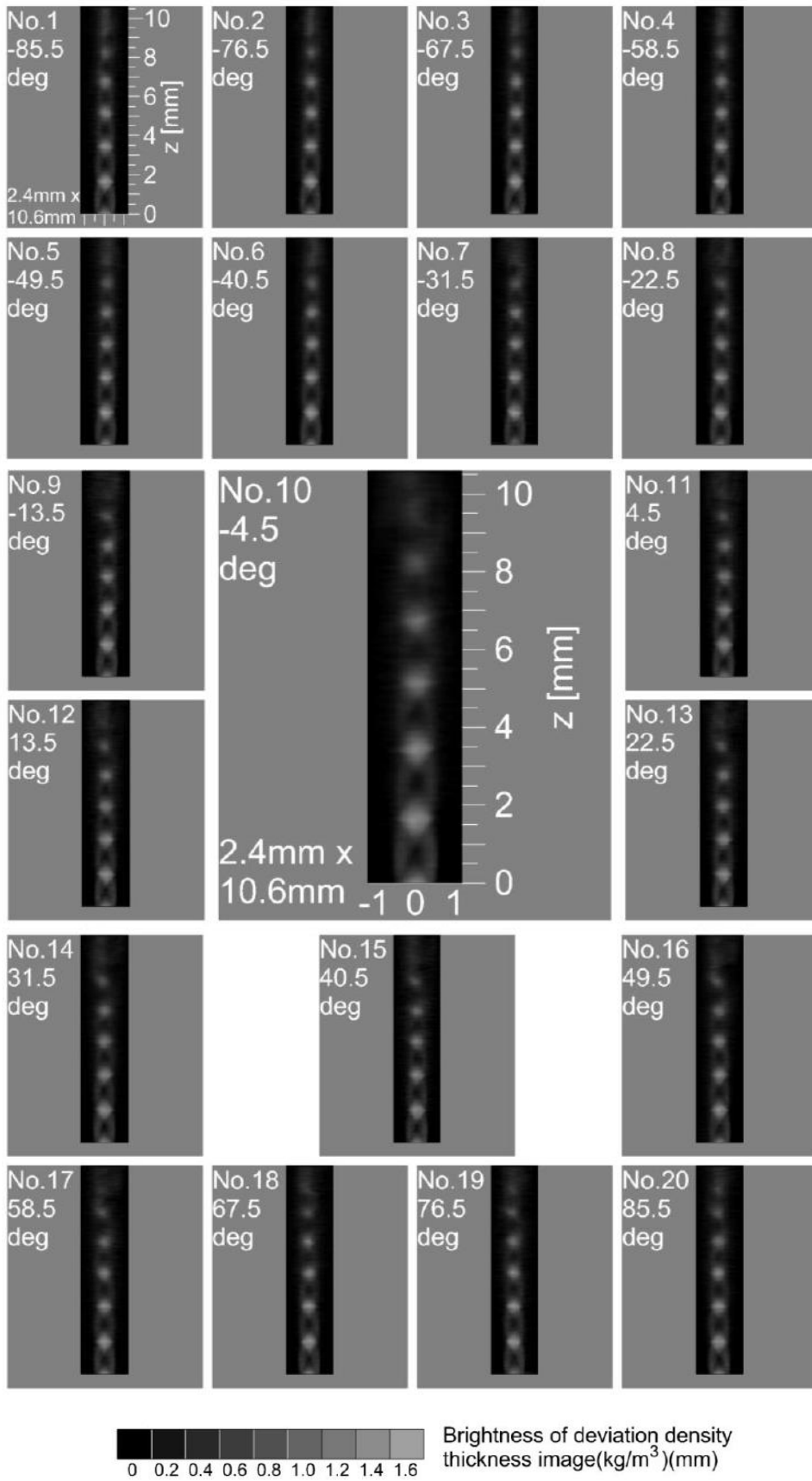
Figure 3.20. Derived density thickness of deviation density thickness (Eq. 3.5) images NPR 5 (Figure 3.18 (h)).
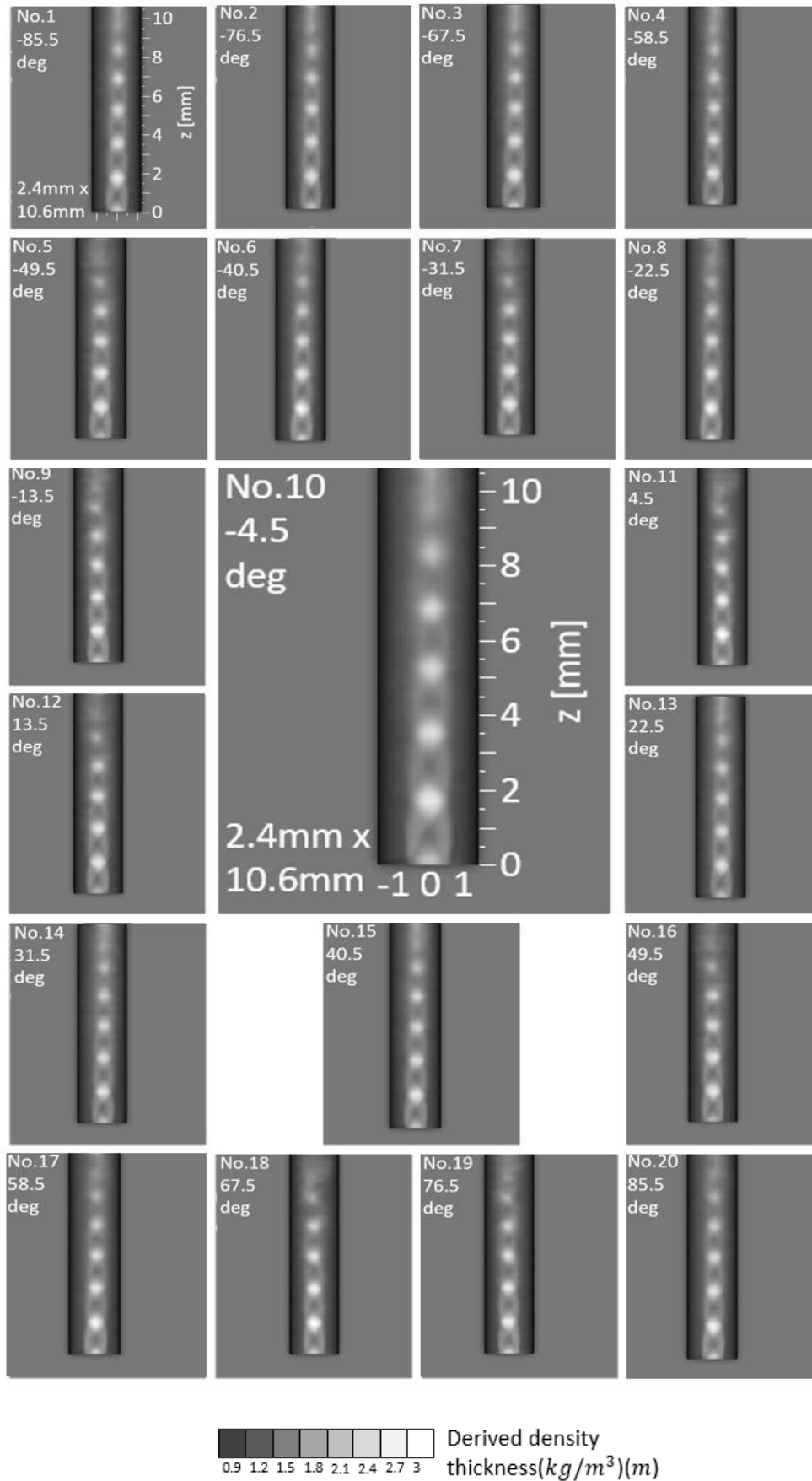
Figure 3.21. Derived density thickness (Eq. 3.6) images NPR 5 (Figure 3.18 (i)).

3.5. CT-reconstruction

Once the derived density thickness is obtained, the ML-EM method for CT-reconstruction can be applied. This reconstruction method is an iterative algorithm, where the projections (or derived density thickness) taken by the 20 cameras of the Schlieren system are used to reconstruct the different cross-section of the target. Projection data values are distributed and arranged in the beam path direction with respect to all reconstructed pixels.

Figure 3.22 shows the notation and coordinated system using in this algorithm which is the same explained in Section 2.3.1. The cross-section is divided in m pixels, whose voxel value is defined as λ_j^k where j is the number of the voxel and k is the number of iteration taken. y_i is the measured projection data at the i-th pixel which correspond with the derived density thickness $Dt'(X(\theta))$ obtained in Section 3.3. Finally, C_{ij} represents the detection probability which is defined as the overlapped volume between i-th ray and the voxel j. In Figure 3.22 (right) there is a representation of the meaning of C_{ij}.
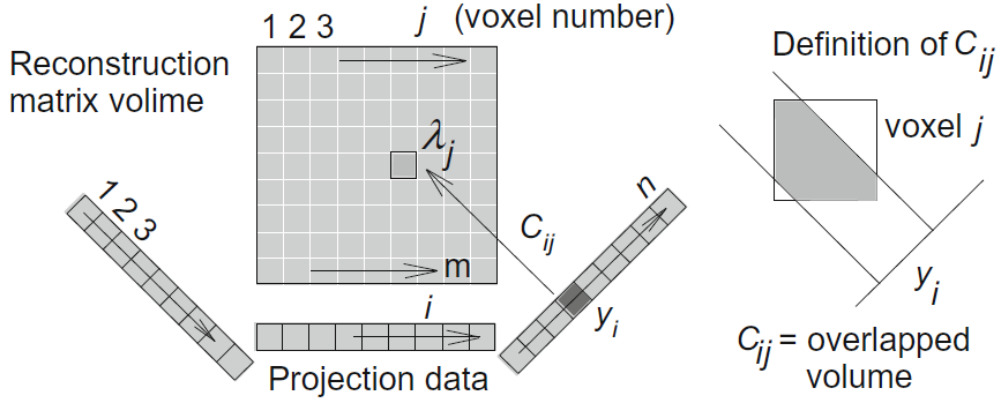
Figure 3.22. Notation and coordinate system for ML-EM reconstruction for 3D volume (Ishino, et al., 2015).

Eq. 3.7, which is the same as Eq. 2.62, is used as iteration method for the calculation of λ_j values.

$$\lambda_j^{k+1} = \frac{\lambda_j^k}{\sum_{j=1}^n C_{ij}} \sum_{i=1}^m \frac{y_{ij}\, C_{ij}}{\sum_{j=1}^n C_{ij}\, \lambda_j^k}$$

Eq. 3.7

The CT algorithm is run in each horizontal plane of z-axis for the reconstruction of deviation density distribution $\Delta\rho(x,y)$ from linear data set of density thickness. Since the values used as projection are $Dt'(X(\theta))$, the result obtained is $(\Delta\rho(x,y) + (\rho_{ref} - \rho_a^*))$ and it is represented in Figure 3.18 (j). It can be observed that $\Delta\rho(x,y)$ distribution obtained in Figure 3.18 (c) and (j) is the same. The only different is that Figure 3.18 (j) is shifted $(\rho_{ref} - \rho_a^*)$ from (c).

Finally, 2D density distribution is obtained as follow.

$$\rho(x,y) = \rho_{ref} - \left[\Delta\rho(x,y) + \left(\rho_{ref} - \rho_a^*\right)\right] = \rho_a^* - \Delta\rho(x,y)$$

Eq. 3.8

$\rho(x,y)$ is represented in Figure 3.18 (k) and its values are the same than in Figure 3.18 (b). Density 2D distributions are accumulated in layers to form 3D-CT density distribution

$(\rho(x,y,z))$. Figure 3.23, Figure 3.24 and Figure 3.25 show the solution of the CT-reconstruction for the planes YZ, XZ and XY respectively.

$\rho \; [kg/m^3]$

0.6 0.9 1.2 1.5 1.8 2.1 2.4 2.7
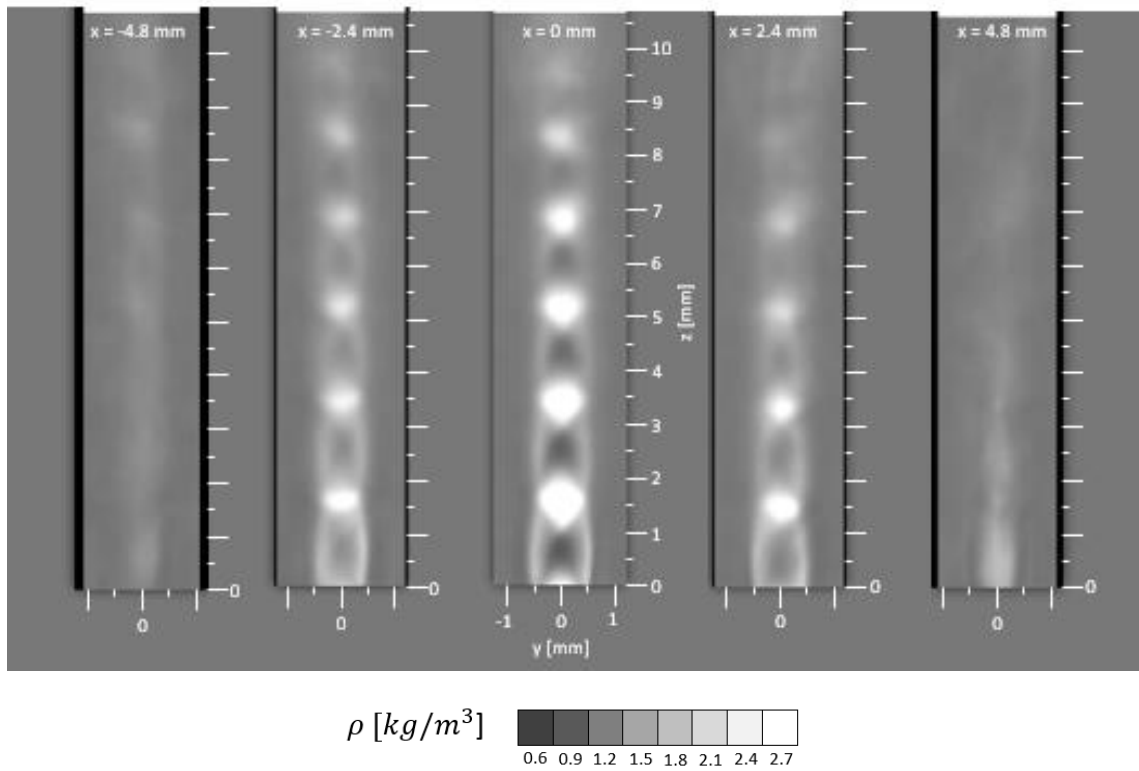
Figure 3.23. YZ plane results of CT-reconstruction for NPR 5.

$\rho \; [kg/m^3]$

0.6 0.9 1.2 1.5 1.8 2.1 2.4 2.7
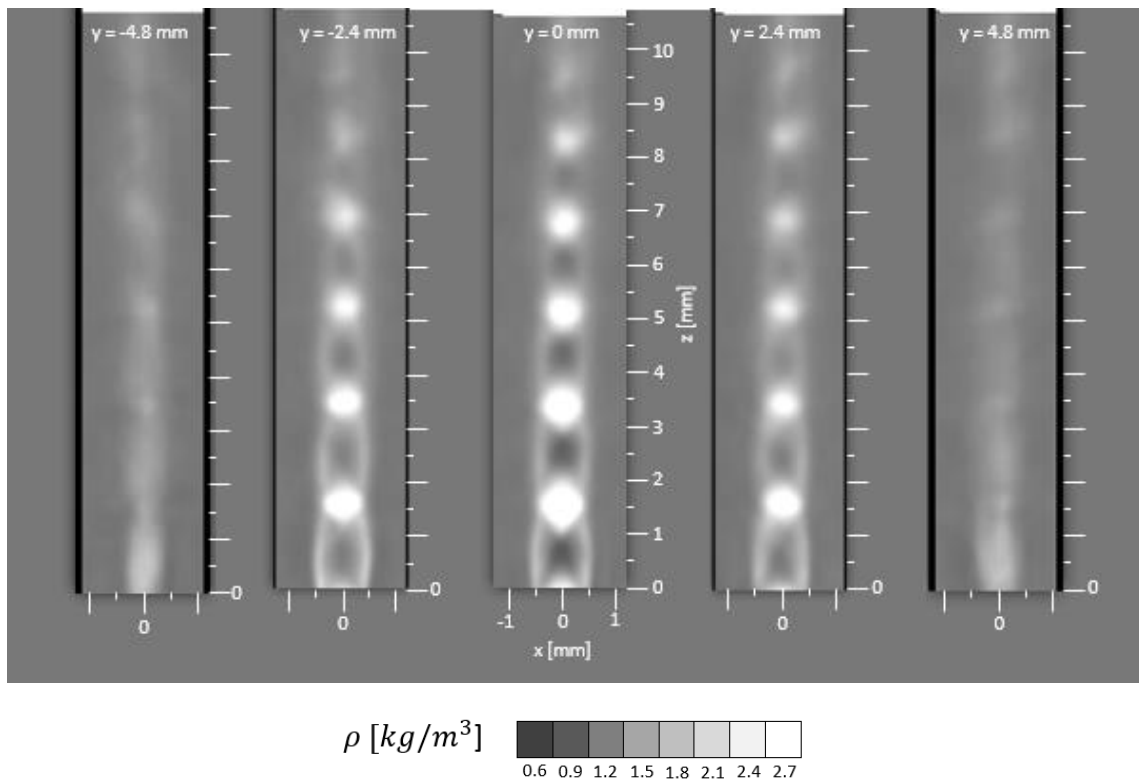
Figure 3.24. XZ plane results of CT-reconstruction for NPR 5.

As it can be observed, the solutions in planes YZ and XY are very similar since the nozzle has a circular shape. The solutions at $x = 0$ and $y = 0$ are very clear and the diamond structure can be observed. As we move away from the centerline and due to the increasing of the mixing layer, the diamond structures start to disappear. Images at 4.8 mm from the centerline are far enough to represent exclusively the mixing layer.
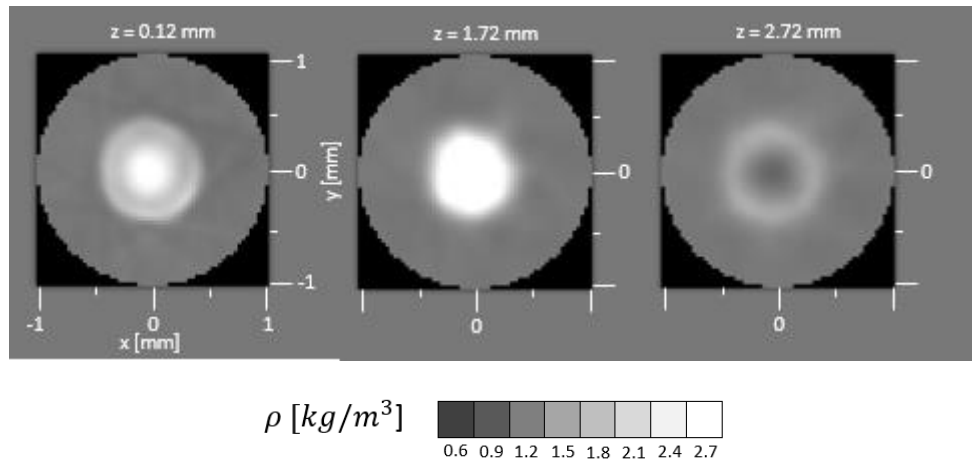
Figure 3.25. XY plane results of CT-reconstruction for NPR 5.

In the results of the XY plane, the jet boundaries can be observed. The jet is surround by a shock wave which change the supersonic flow condition to atmosphere condition. At $z = 0.12 \, mm$ a cross-section of the incident shock is represented.

4. Results

4.1.   Model Validation

Before applying the numerical method implemented in the present study to our experimental data, it is needed to probe if the code works properly. Comparisons are done with the numerical method presented by (Cheng & Lee, 2005), the analytical solution of (Jackson & Tam, 1985) and the experimental data of (Seiner & Norum, 1979). Initial conditions are summarized in Table 4.1.

Ambient Temperature	T_b	288 K (15 ºC)
Back (ambient) pressure	P_b	0.101325 MPa
Back (ambient) density	ρ_b	1.2 kg/m^3
Nozzle design Mach number	M_d	1.73
Nozzle exit Mach number	M_e	2
Nozzle exit diameter	D	50 mm
Exit pressure	P_e	0.146920 MPa
Exit density	ρ_e	3.2 kg/m^3
Exit axial-velocity	u_e	507 m/s
Exit radial-velocity	v_e	0 m/s

Table 4.1. Initial condition of (Seiner & Norum, 1979) experimental data.

The results of instantaneous pressure, density and Mach number at a representative dimensionless time, $t_d = t/(D/u_e) = 125$, are shown Figure 4.1. The structure observed is similar to what can be expected in an underexpanded jet, explained in Section 2.1.2.1.

In density and pressure fields (Figure 4.1 (left) and (center)) the characteristic diamond-shape shocks cell can be clearly observed. Prandtl-Mayer expansion fans are formed at the nozzle exit, reflecting the flow forth the centerline. Afterward, oblique shocks are generated from the free shear layer to direct the flow back to the center line. This structure is repeated until $z/D = 17$, where the ambient air enters into the jet. At that point, there is not enough energy to keep the structures and the phenomenon die out. Regarding the Mach (Figure 4.1 (right)), no normal shock can be observed in the near field of shock containing region. Subsonic Mach numbers are represented with cold colors, whereas supersonic Mach number with hot.

The mean streamwise pressure variations along the x-axis in the underexpanded jet of the present study is compared with three diferent approaches to verify the method accuracy. Figure 4.2 shows the comparison beteween the numerical method implemented in this study and the Prandtl model explained in Section 2.1.2.2. We can observe there is a good agreement in the period but not in the value of the pressure away from the first cycles. However, this is what can be expected, due to the two main drawbacks of the model. Firstly, the model only works close to the nozzle exit, and secondly, since deadening due to turbulence is not considered, the amplitude is constant.

The numerical method implemented by (Cheng & Lee, 2005) is represented in Figure 4.3. I great agreement between the two numerical method can be observed. Both methods exhibit a decaying oscillatory static pressure caused by the interaction between the shock cells and the mixing layer near the edge of the flow.
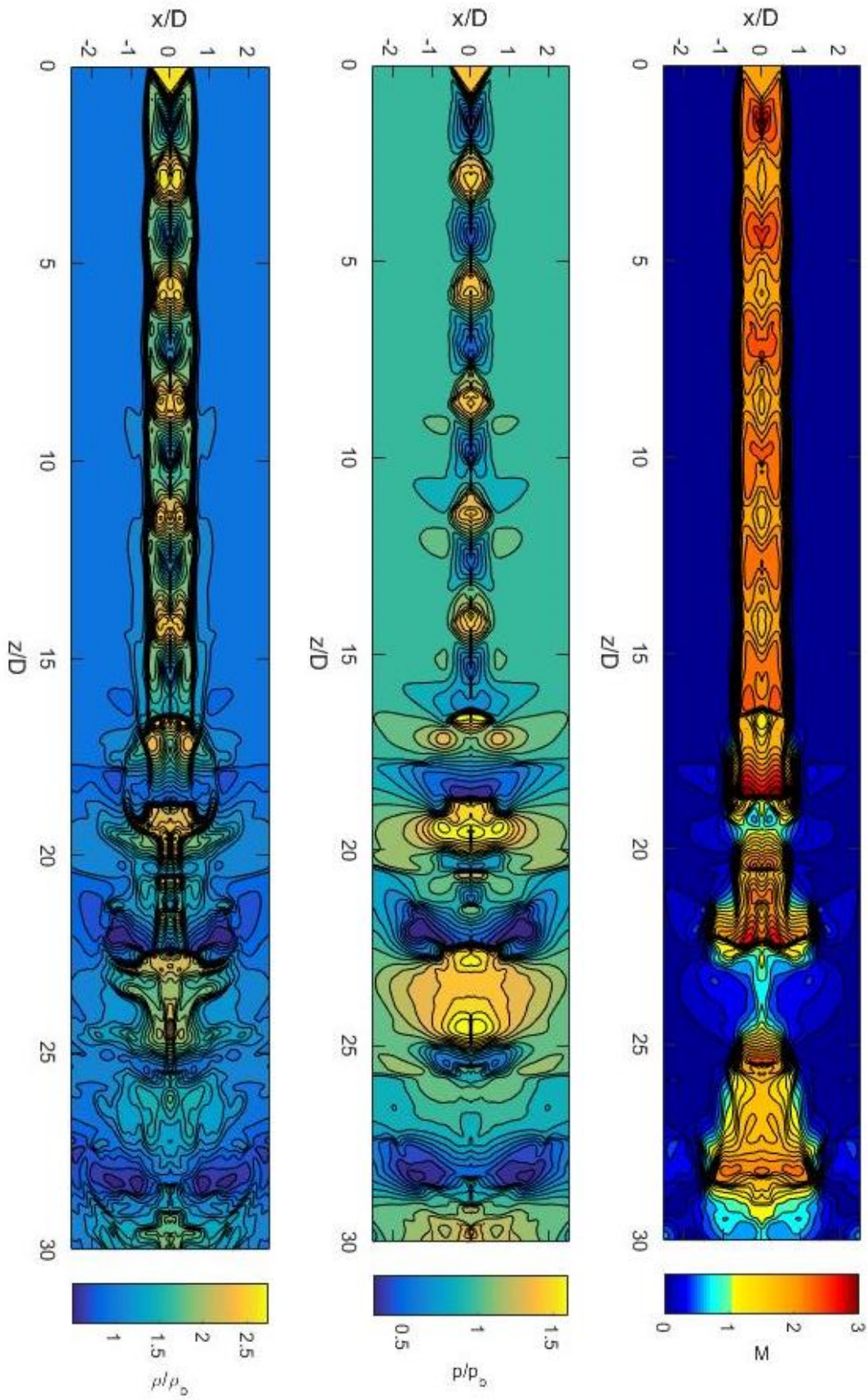
Figure 4.1. Instantaneous Flow pictures for underexpanded jet at dimensionless time $t_d = 125$: (left) density (contour lines from 0.6 to 2.6), (center) pressure (contour lines from 0.3 to 1.6), (right) Mach number (contour lines from 0 to 3).
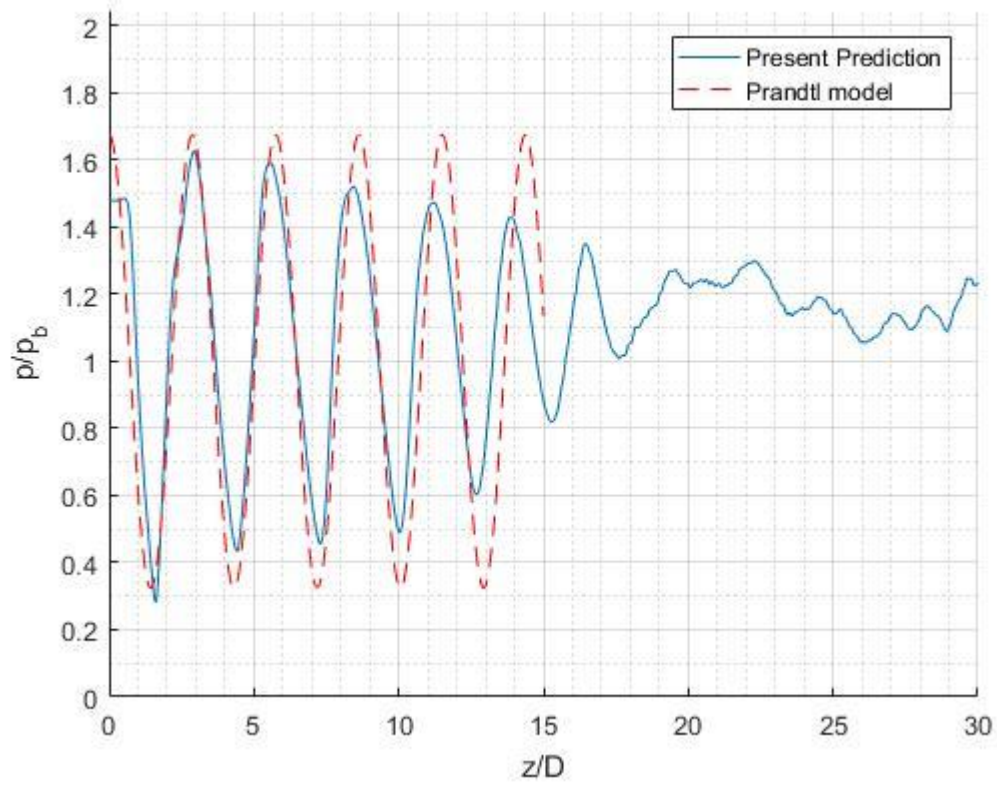
Figure 4.2. Comparation of the present numerical method with Prandtl model of Section 2.1.2.2.
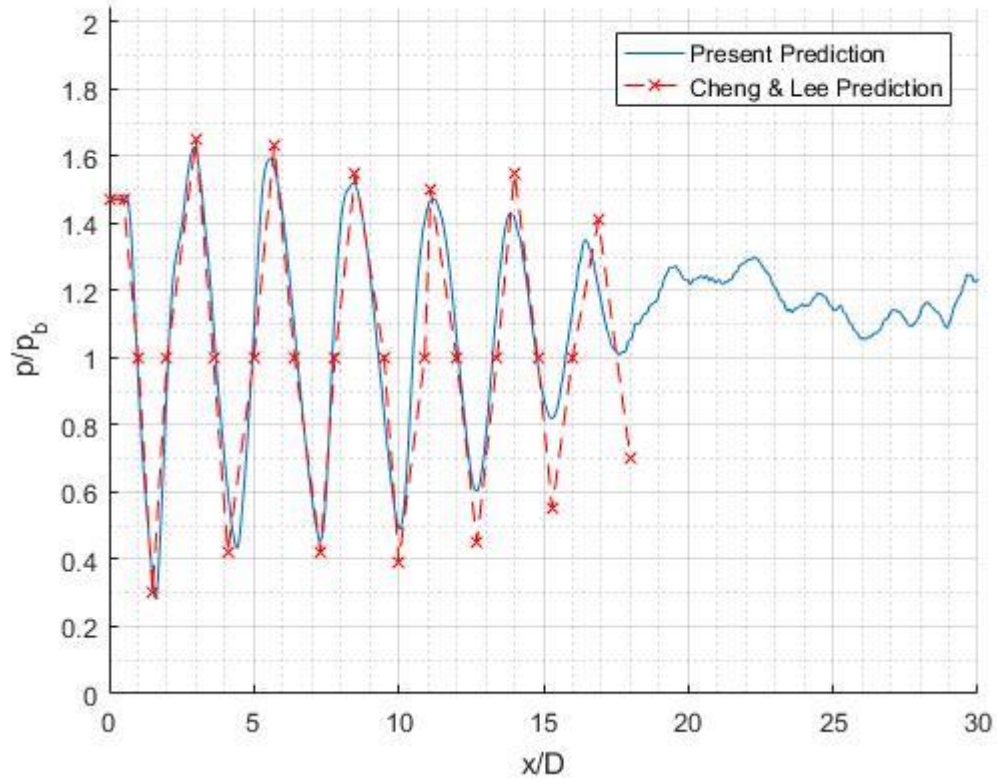
Figure 4.3. Comparation of the present numerical method with the numerical method developed by (Cheng & Lee, 2005).

The present calculation agrees quite well in the first 5 diamond-shape structures with the experiment of (Seiner & Norum, 1979) represented in Figure 4.4, even though the method underestimate the pressure. At this range, the flow can be considered inviscid. Farther downstream, there are differences in the predicted data with the experimental. The present method also underestimates the rate of mixing between the jet and the ambient fluid.
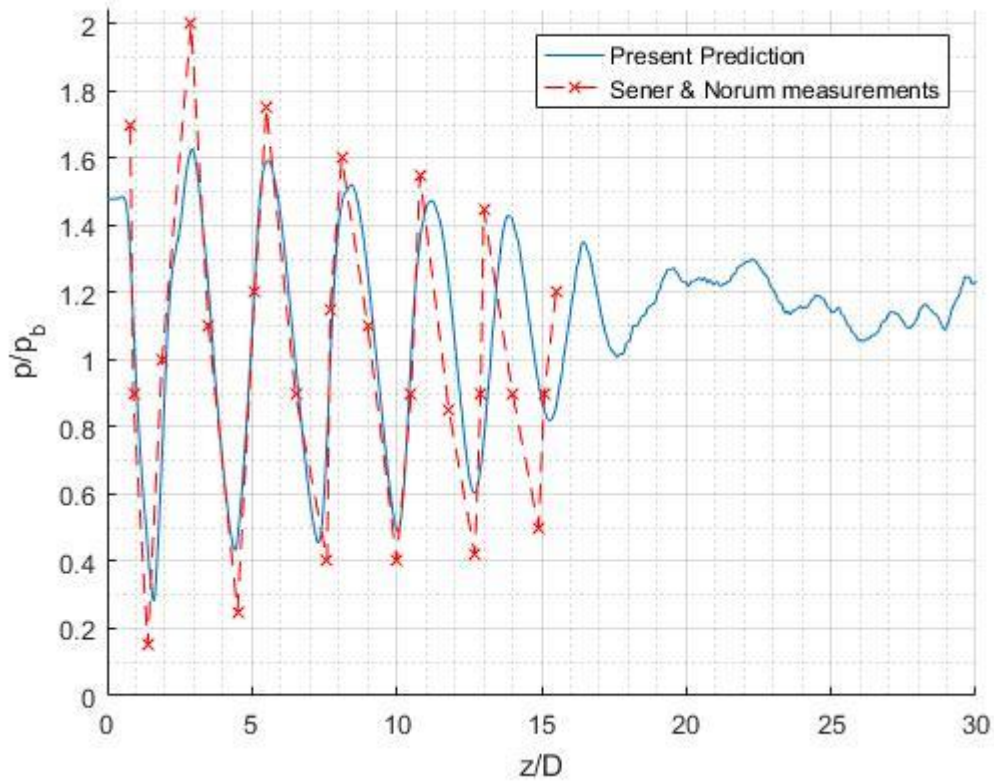
Figure 4.4. Comparation of the present numerical method with the measurements of (Seiner & Norum, 1979).

A radial study of Mach number has been carried out in order to compare the present method along the x-axis with (Seiner & Norum, 1979) and (Cheng & Lee, 2005) results. Figure 4.5 shows the radial solution at different values of z/D. I great agreement can be observed in general for the three approaches. The locations of the discontinuities in the flow are properly captured.

Nevertheless, mismatches around the jet center-line and boundaries can be observed between the predicted and the experimental data. The nozzle measured by (Seiner & Norum, 1979) had a converging-diverging shape. However, in the numerical method implemented, the flow is assumed to be parallel. The converging-diverging nozzle expands jet plume to an outer radial region than does a tube nozzle, thus it causes a slower decaying rate of Mach number in the jet boundary. The consequence is an underprediction of the Mach number in the mentioned regions.
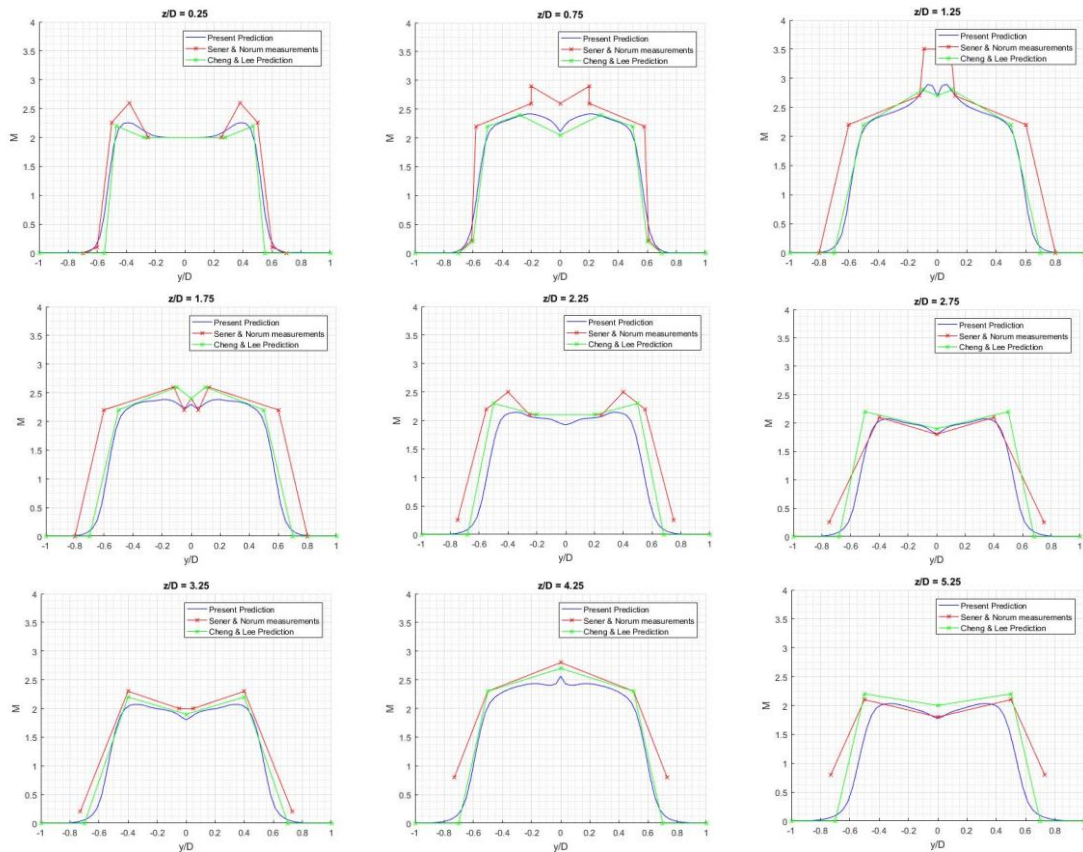
Figure 4.5. Comparation of present prediction, (Cheng & Lee, 2005) prediction and (Seiner & Norum, 1979) measurement of the radial distribution of Mach number at various axial positions in the underexpanded jet.

4.2.   Comparison of numerical and experimental results

In this section we are going to compare the results of the numerical method implemented in the present study with the experimental measurements obtained using the multi-directional quantitative Schlieren system. We are going to display the solution for NPR 5, 4.5 and 4. The values of JPR of each condition are 1.362, 1.226 and 1.09 respectively. Initial conditions of the three different study are summarized in Section 3.2.

4.2.1. Flow images

In order to achieve a better understanding of the flow characteristics of the three initial conditions, density fields are displayed in Figure 4.6. These results are calculated averaging the instantaneous results among the interval $[100 < t_d < 125]$. The scale used in the three images is the same (contour lines from 0.4 to 1.7).

In the images, the values where the instabilities appear can be clearly observed. For NPR 5 this value is $z/D = 18$, for NPR 4.5 is $z/D = 16$ and for NPR 4 is $z/D = 11$. Until this point, the characteristic diamond structures of the underexpanded flows are clearly observed. Beyond these points, the mixing layer start developing. The present numerical method works properly in areas where the flow is largely inviscid, so it will predict the results accurately close to the nozzle exit. However, it underestimates the development of the mixing layer; therefore, far from the nozzle exit numerical results will differ from experimental data.

45
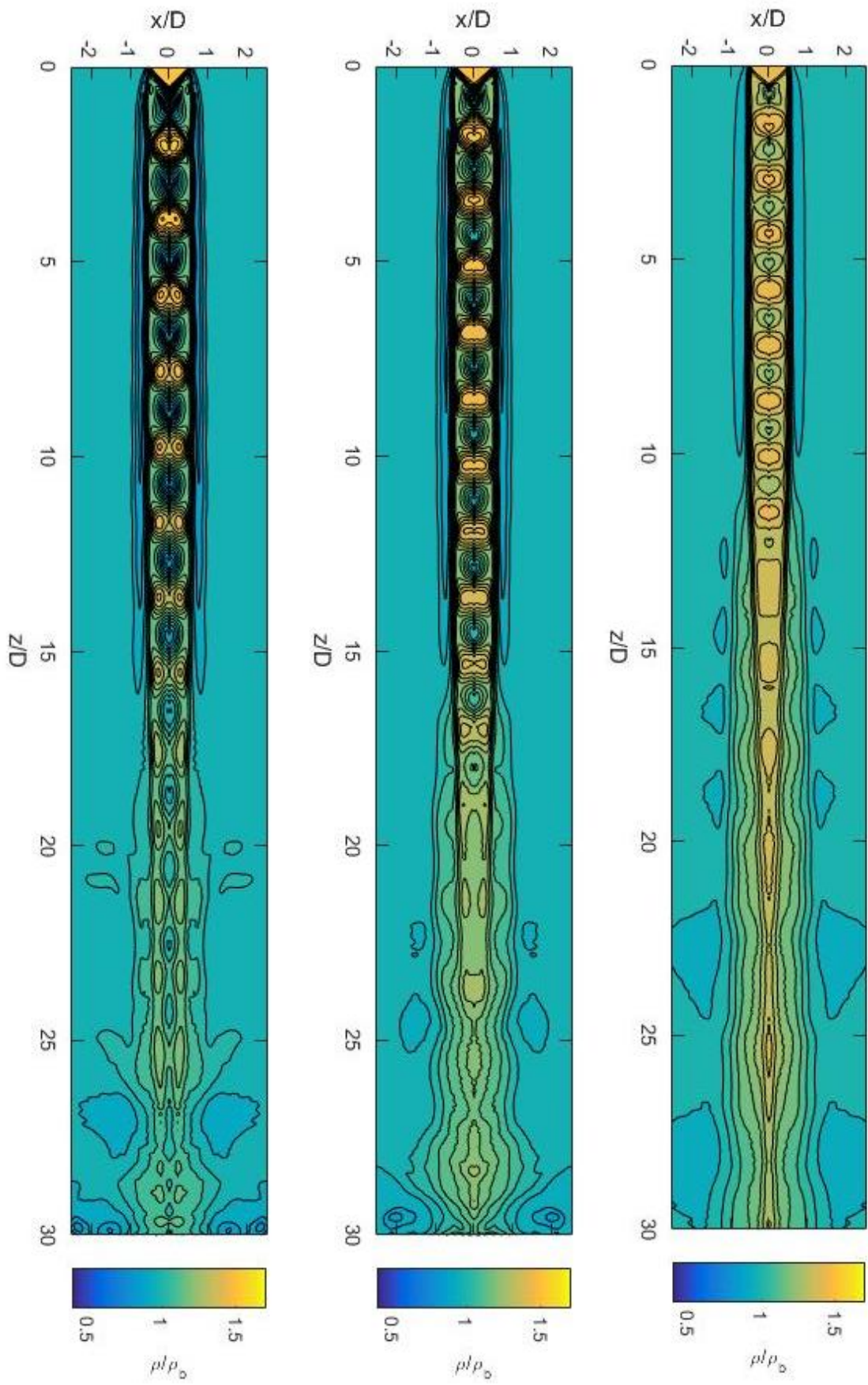
Figure 4.6. Density flow images for underexpanded jet averaging between $100 < t_d < 125$ (contour lines from 0.4 to 1.7): (left) NPR 5, (center) NPR 4.5, (right) NPR 4.

It can be observed there is not flow mixing between the jet and the ambient flow until the instability point is reached. This would impede its applications to supersonic combustion in which mixing of fuel and oxidizer is extremely important.

Finally, Figure 4.7 shows simultaneously the solution of the numerical method and an image of the supersonic jet at NPR 5 obtained with CT-reconstruction at $y = 0$. A good agreement can be observed between both solution in the cells close to nozzle exit, but solutions differ further downstream.
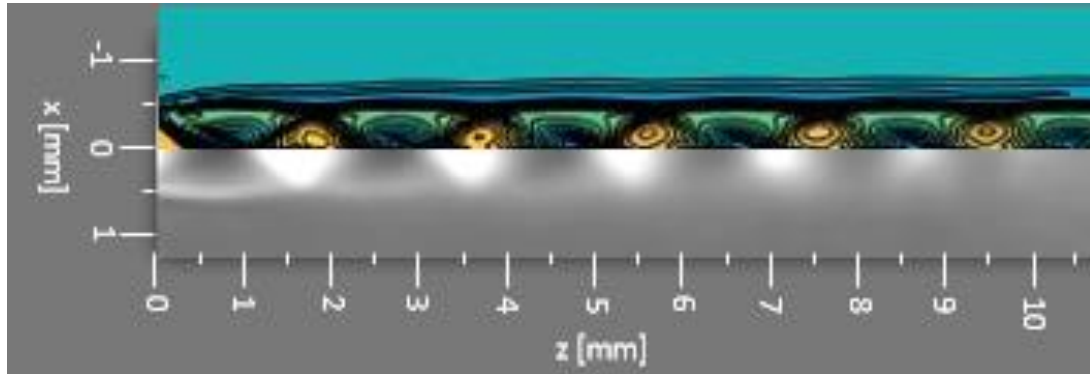
Figure 4.7. Comparison of CT-reconstruction solution image at $y = 0$ with numerical prediction (NPR 5).

4.2.2. Comparation with Prandtl model

Prandtl model is going to be use with the objective to verify the validity of the numerical method before applying it to the experimental results. In Section 4.1, we saw that Prandtl model agrees in the period and in the first pressure values.
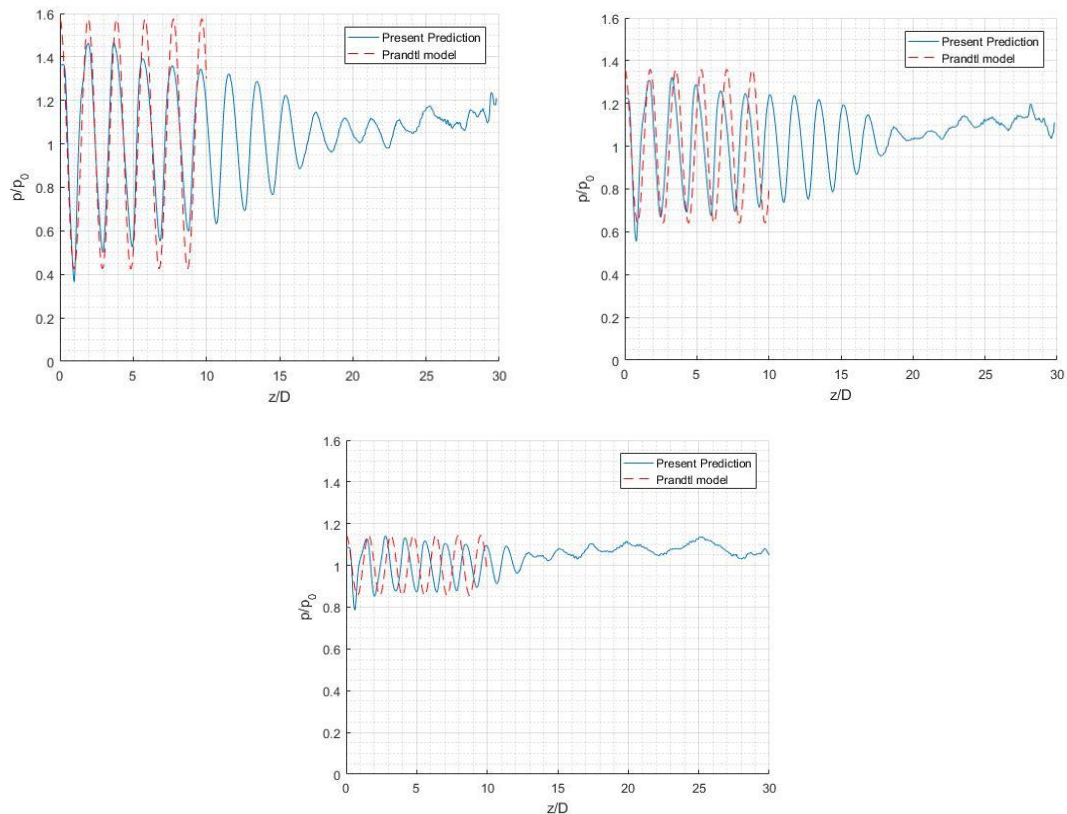
Figure 4.8. Prandtl model: (left) NPR 5, (right) NPR 4.5 and (down) NPR 4.

Figure 4.8 shows the Prandtl model for NPR 5, 4.5 and 4 respectively. As it was expected, there are good agreements within the periods and the first values of pressure. However, whilst NPR 5 solution fit quite well, NPR 4 is not as accurate. This can be explained regarding the drawbacks of Prandtl model, since it is expected for the mixing layer in NPR 4 to develop earlier and Prandtl model makes accurate prediction with thin mixing layer.

4.2.3. Axial comparation

In this section we are going to display the axial results of the numerical method, comparing them with the experimental measurements (Figure 4.9). We can observe a poor agreement in terms of amplitude among the solutions of both studies. However, there is a good agreement in the period, especially in cells close to the nozzle exit.
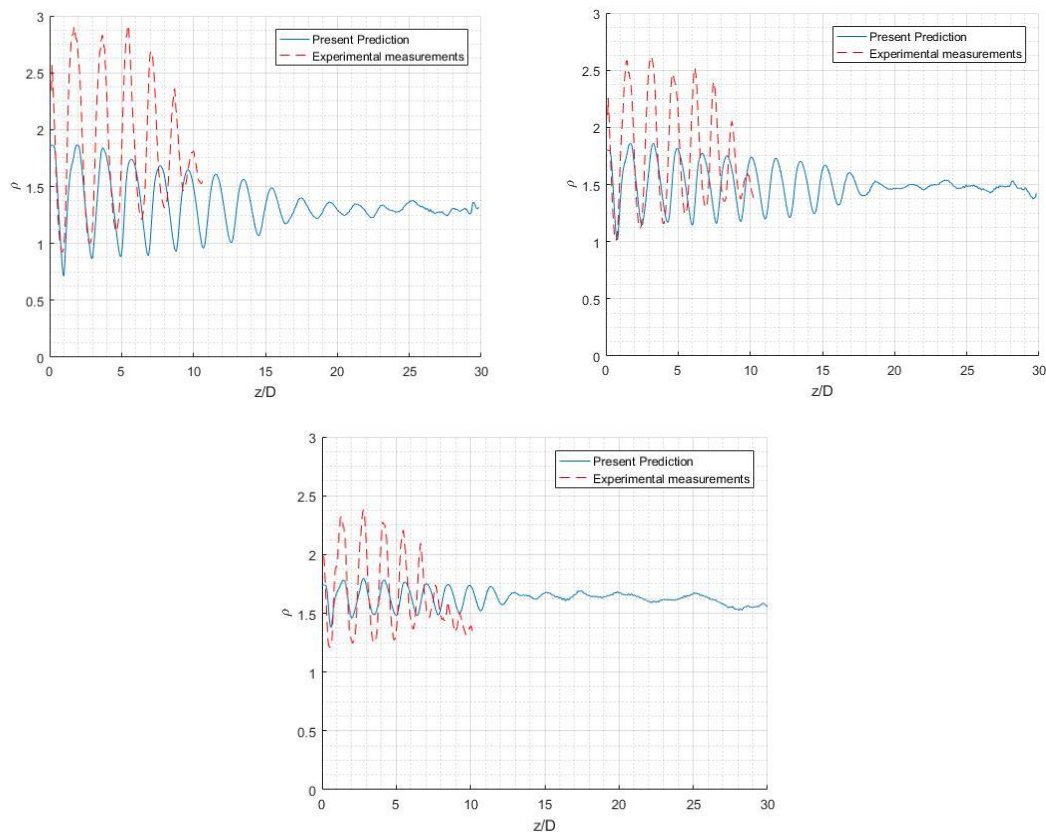
Figure 4.9. Axial comparation: (left) NPR 5, (right) NPR 4.5 and (down) NPR 4.

In Section 4.1, it has been proved the numerical method underestimate the peaks and valleys values. However, the absolute difference between numerical data and CT-reconstruction is too high. One possible explanation to this inconsistence is that CT-reconstruction use a gray-scale (Figure 3.17) where the limits of this scale are imposed manually and may be overestimated. The solution of this inconsistence involves a review of the FORTRAN® code used in CT-reconstruction to adjust the density values of the gray-scale. However, this goes beyond the objectives of the present study and it is proposed as future work.

4.2.4. Radial comparation

The radial results for $z/D = 1, 1.5 \text{ and } 2$ are represented for the three initial conditions in Figure 4.10, Figure 4.11 and Figure 4.12 respectively. We can observe measured density values differs from the calculated. However, the tendency that density follows in each case is the same. This is consequence of the gray-scale used as it was commented before.
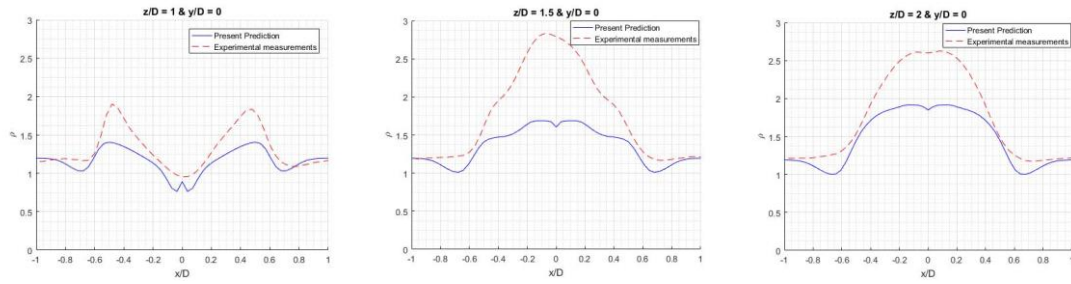
Figure 4.10. Radial comparison for NPR 5: (left) $z/D = 1$, (center) $z/D = 1.5$ and (right) $z/D = 2$.
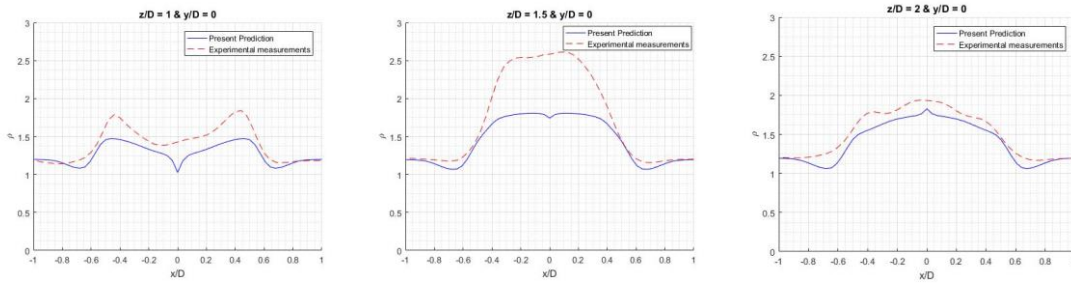
Figure 4.11. Radial comparison for NPR 4.5: (left) $z/D = 1$, (center) $z/D = 1.5$ and (right) $z/D = 2$.
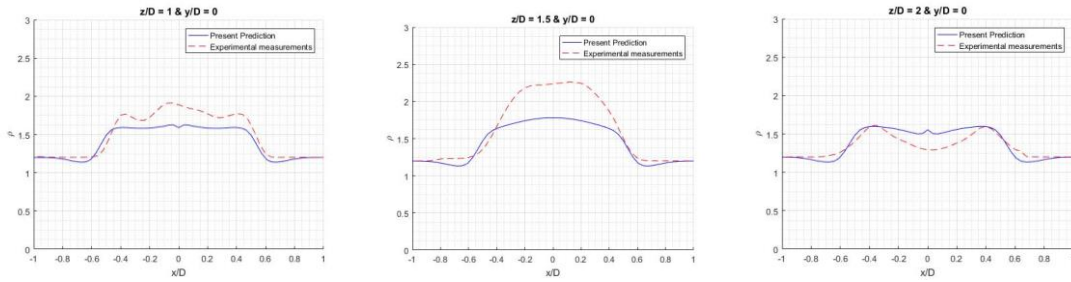
Figure 4.12. Radial comparison for NPR 4: (left) $z/D = 1$, (center) $z/D = 1.5$ and (right) $z/D = 2$.

The peaks which appear in all the images at $x/D = 0$ is consequence of the symmetric condition imposed at that point.

4.2.5.   Cell spacing

We are going to compare the cell length of the first shock using Prandtl's formula (Eq. 2.15) with the images obtained with CT-reconstruction and the numerical simulation. Figure 4.13 shows the Schlieren images for NPR 4, 4.5 and 5 respectively. In these images the first cell length is indicated with a black line.

In order to make a comparison, numerical values are needed. The first shock cell of the different jet covers the interval between the origin and the first maximum of Figure 4.9. The length cell values of the experimental measurements are obtained counting the number of pixels present among the interval and multiplying it times $0.04\ mm/pixel$ (in dimensionless unit $0.04\ pixel^{-1}$ since the diameter is $1\ mm$).

Results are presented in Table 4.2. It can be observed when NPR is higher the cell length increases. This relation can be observed in Eq. 2.15. NPR is a direct function of the Mach number (Eq. 2.8) and the Mach number is proportional to the cell length. Therefore, the next statement can be done:

$$L_s \propto M$$
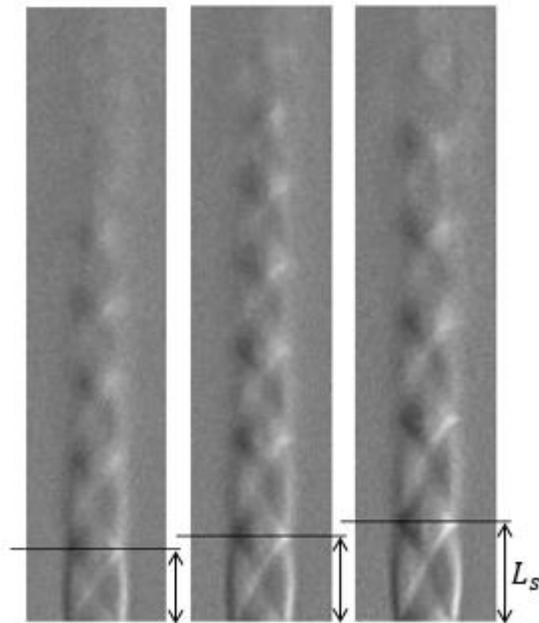
Figure 4.13. Cell length of Schlieren images of the underexpanded supersonic micro-jet: (left) NPR 4, (center) NPR 4.5, (right) NPR 5.

Nozzle pressure ratio (NPR)		**5.0**	**4.5**	**4.0**
Prandtl's formula (Eq. 2.15)		1.81	1.69	1.56
Schlieren images	Nº Pixels	45	38	34
	L_c	1.80	1.52	1.36
Numerical method		1.93	1.63	1.51

Table 4.2. First shock cell length.

The difference between the numerical method and the measurement over the Schlieren images is around 10%, which is a very reasonable error giving the simplification imposed.

5.   Conclusions

In the present project we have implemented a numerical method using WENO schemes with fifth-order-accurate for spatial discretization and fourth-order-accurate Runge-Kutta scheme for time integration. The code can predict the flow structure of a supersonic jet working at underexpanded condition. The validity of the present method has been proved using an analytical solution known as Prandtl model (Jackson & Tam, 1985), (Seiner & Norum, 1979) data and (Cheng & Lee, 2005) prediction.

Prandtl solution's drawback is overcome using the present method, since the objective was to create a method which takes into account the expansion of the mixing layer and the reduction of the amplitude. However, the present method still does not work accuracy enough far from the nozzle exit as it is shown in Figure 4.4 and Figure 4.7 where the predicted density concentration does not fit with the measured. The present method underestimates the mixing layer development since Euler equations (Eq. 2.17 and Eq. 2.18) are an inviscid solution for the problem.

Other methods used in Computational Fluid Dynamic such as k-ϵ could enhance the solution. k-ϵ method is a turbulent model which could make a better estimation of the mixing layer. However, the implementation of this method is quite more difficult, the time required to obtain an accurate solution is much higher and a computer with a better processing speed is needed.

The present numerical method is compared with the measurement of a circular supersonic jet using a multi-directional quantitative Schlieren system. The measurements were expected to fit relatively well with the calculation. However, Figure 4.9 shows that there is a great difference between the two solutions. Prandtl model as well as the validation process show in Section 4.1 make possible to rely on the numerical method solutions. The period of oscillations in Figure 4.9 coincide, the main difference resides in the amplitude of the oscillation. The conclusion of this phenomenon is that the values of the limits given to the gray-scale used in CT-reconstruction might be overestimated. Therefore, a re-adjustment it is needed to be done in CT-reconstruction code.

The present study was focused on the simulation of a circular supersonic micro-jet working at underexpanded condition. However, some experimental data have been obtained using a rectangular cross-section nozzle. The present numerical method can be modified to simulate this cross-section by giving to the vector S in Eq. 2.18 a value which simulate the rectangular cross-section.

6. Bibliography

Anderson, J. D. (1982). *Modern compressible flow with historical perspective.* McGraw-Hill Book Company.

Bruyant, P. (2018, March). *Analytic and Iterative Reconstruction Algorithms in SPECT*. Retrieved from http://jnm.snmjournals.org/content/43/10/1343.full

Chen, K. (1998). Numerical simulation and noise supression of high speed jet. *PhD thesis.* Taiwan: Institute of aeronautics and astronautics, national Chen Kung University.

Cheng, T., & Lee, K. (2005). Numerical simulation of underexpanded supersonic jet and free shear layer using WENO schemes. *International Journal of Heat and Fluid Flow 26*, (pp. 755-770).

Dash, S., Wolf, D., & Seiner, J. (1985). Analysis of turbulent underexpanded jet. *part I: parabolized NAvier Stokes model* (pp. 505-514). SCIPVIS, AIAA.

Foelsch, K. (1949). *The Analytical Design of an Axially Symmetric Laval Nozzle for a Parallel and Uniform Jet.* J. Aeronautical Sciences.

Fukuda, H., Maeda, H., Ono, D., Nakao, S., Miyazato, Y., & Ishino, Y. (2016). *Rainbow Schlieren Measurements in Underexpanded Jets from Axisymmetric Supersonic Micho Nozzel.* Honolulu: The 27th International Symposium on Transport Phenomena.

Gonzalez, R. C., & Woods, R. E. (2008). *Digital image proccesing, 3º edition.* New Jersey: Pearson Education.

Ishino, Y., Hayashi, N., Ishiko, Y., Nazari, A. Z., Nagase, K., Kakimoto, K., & Saiki, Y. (2016). *Schlieren 3D-CT reconstruction of instantaneous density distributions of spark-ignited flame kernels of fuel-rich propane-air premixture.* Washington DC: Summer Heat Transfer Conference.

Ishino, Y., Hayashi, N., Razak, I., Kato, T., Kurimoto, Y., & Saiki, Y. (2015). *3D-CT (Computer Tomography) Measurement of an Instantaneous Density Distribution of Turbulent Flames with a Multi-Directional Quantitative Schlieren Camera (Reconstructions ofHigh-Speed Premixed Burner Flames with Different Flow Velocities).* Springer.

Ishino, Y., Horimoto, K., Kato, T., Ishiguro, S., & Saiki, Y. (2013). *3D-CT Measurement of Premixed Flames Using a MultiDirectional Quantitative Schlieren Optical System (Solo-Measurement of Density and Combined-Measurementof Density and Light-Emission distributions).* Nagoya: 7th Asian-Pacific Conference on Aerospace Technology and Science.

Jackson, J. A., & Tam, C. (1985). *On the Shock Cell Structure And Noise Of Imperfectly Expanded Supersonic Jets.* Florida: The florida state university college of arts and science.

Jiang, G., & Shu, C. (1996). Efficient Implementation of Weighted ENO Schemes. *Journal of Computational Physics*, (pp. 202-228).

Lekholm, V. (2012). *Schlieren imaging of microthruster exhausts for qualitative and quantitative analysis.* Measurement Science and Technology.

Marton, L., & Marton, C. (1981). *Methods of Experimental Phuysics. Part A.* Bethlehem: Academic Press.

Merzkirch, W., & Gersten, K. (1987). *Techniques of flow visualization.* Seine: North Atlantic Treaty Organization.

Nazari, A. (2017). *3D-CT (Computer tomography) measurement of 3D distributions of instantaneous density of the shock-cell structure of underexpanded supersonic micro-jets with 20-directional Schlieren camera.* Nagoya: Nagoya Institute of Technology.

Nazari, A. Z., Ishino, Y., Ishiko, Y., Motohiro, T., Yamada, R., Saiki, Y., . . . Nakao, S. (2017). *Schlieren CT measurement of 3D density distributions of perfectly and imperfectly expanded supersonic micro-jets from circular and rectangular micro nozzles.* Okinawa: The 9th JSME-KSME Thermal and Fluids Englineering Conference.

Nazari, A. Z., Ishino, Y., Motohiro, T., Yamada, R., Ishiko, Y., & Saiki, Y. (2017). *Schlieren CT Measurement of 3D Density Distribution of Flame Kernels of Spark-Ignited Direct-Injection of Free, Cavity-Guided and Plane-Guided Fuel Jets.* Sydney: 11th Asia-Pacific Conference on Combustion.

Penczek, P. A. (2011, 10 2). *Fundamentals of three-dimensional reconstruction from projections*. Retrieved from https://www.ncbi.nlm.nih.gov/pmc/articles/PMC3165033/

Powell, A. (2009). On Prandtl's formulas for supersonic jet cell length. University of Houston.

Šámal, M. (2004, April). *SPECT reconstruction*. Retrieved from http://www.dtic.upf.edu/~afrangi/ibi/ReconstructionFromProjections.pdf

Seiner, J. M., & Norum, T. D. (1979). Experiments of shock associated noise on supersonic jets. AIAA paper 79-1526.

Appendix 1. Jacobian Matrix

The development of the Jacobian Matrix used in Eq. 2.25 is explained in this section. A Jacobian matrix is a matrix of all first-order partial derivatives of a vector-valued function ($F(W)$). We want to calculate the Jacobian matrix of $F(W)$ with the variables in W (the process to calculate the Jacobian matrix of the flux $G(W)$ is similar).

$$W = \begin{bmatrix} \rho \\ \rho u \\ \rho v \\ e \end{bmatrix}, F(W) = \begin{bmatrix} \rho u \\ \rho u^2 + p \\ \rho uv \\ (e + p)u \end{bmatrix}$$

For that, W is going to be redefined as:

$$W = \begin{bmatrix} \rho \\ \rho u \\ \rho v \\ e \end{bmatrix} = \begin{bmatrix} \lambda_1 \\ \lambda_2 \\ \lambda_3 \\ \lambda_4 \end{bmatrix}$$

Eq. 0.1

And the equation of state (Eq. 2.19) as:

$$p = (\gamma - 1)\left(\lambda_4 - 0.5\left(\frac{\lambda_2^2}{\lambda_1} + \frac{\lambda_3^2}{\lambda_1}\right)\right)$$

Eq. 0.2

Therefore, we can rewrite the flux in terms of Eq. 0.1 and Eq. 0.2.

$$F(W) = \begin{bmatrix} \rho u \\ \rho u^2 + p \\ \rho uv \\ (e + p)u \end{bmatrix} = \begin{bmatrix} \lambda_2 \\ (1.5 - 0.5\gamma)\frac{\lambda_2^2}{\lambda_1} + (\gamma - 1)\lambda_4 - 0.5(\gamma - 1)\frac{\lambda_3^2}{\lambda_1} \\ \frac{\lambda_2\lambda_3}{\lambda_1} \\ \gamma\frac{\lambda_4\lambda_2}{\lambda_1} - 0.5(\gamma - 1)\frac{\lambda_2^3}{\lambda_1^2} - 0.5(\gamma - 1)\frac{\lambda_3^2\lambda_2}{\lambda_1^2} \end{bmatrix}$$

The Jacobian matrix to solve is the following.

$$J_F(W) = \begin{bmatrix} \dfrac{\partial F_1}{\partial \lambda_1} & \cdots & \dfrac{\partial F_1}{\partial \lambda_4} \\ \vdots & \ddots & \vdots \\ \dfrac{\partial F_4}{\partial \lambda_1} & \cdots & \dfrac{\partial F_4}{\partial \lambda_4} \end{bmatrix}$$

The solution in terms of λ is presented below.

$$J_F(W)$$

$$= \begin{bmatrix} 0 & 1 & 0 & 0 \\ -(1.5 - 0.5\gamma)\frac{\lambda_2^2}{\lambda_1^2} + 0.5(\gamma-1)\frac{\lambda_3^2}{\lambda_1^2} & (3-\gamma)\frac{\lambda_2}{\lambda_1} & -(\gamma-1)\frac{\lambda_3}{\lambda_1} & (\gamma-1) \\ -\frac{\lambda_2\lambda_3}{\lambda_1^2} & \frac{\lambda_3}{\lambda_1} & \frac{\lambda_2}{\lambda_1} & 0 \\ -\gamma\frac{\lambda_4\lambda_2}{\lambda_1^2} + (\gamma-1)\frac{\lambda_2^3}{\lambda_1^3} + (\gamma-1)\frac{\lambda_3^2\lambda_2}{\lambda_1^3} & -1.5(\gamma-1)\frac{\lambda_2^2}{\lambda_1^2} - 0.5(\gamma-1)\frac{\lambda_3^2}{\lambda_1^2} & -(\gamma-1)\frac{\lambda_3\lambda_2}{\lambda_1^2} & \gamma\frac{\lambda_2}{\lambda_1} \end{bmatrix}$$

Finally, the solution in terms of the flux variables.

$$J_F(W)$$

$$= \begin{bmatrix} 0 & 1 & 0 & 0 \\ -(1.5 - 0.5\gamma)u^2 + 0.5(\gamma-1)v^2 & (3-\gamma)u & -(\gamma-1)v & (\gamma-1) \\ -uv & v & u & 0 \\ -\gamma\frac{eu}{\rho} + (\gamma-1)u^3 + (\gamma-1)u^2 v & -1.5(\gamma-1)u^2 - 0.5(\gamma-1)v^2 & -(\gamma-1)uv & \gamma u \end{bmatrix}$$

Eq. 0.3

Eq. 0.3 is used to calculate the value of β which appears in Eq. 2.24.

Appendix 2. WENO code

In this appendix the code implemented to simulate the supersonic jet using the WENO algorithm is shown below. This code consists of the following functions:

1. main_WENO.m: it is the main program and the one which must be run to start the calculation. Runge Kutta 4 step is implemented in the while loop. All the initial condition and the saving file path must be changed here.
2. initial_condition.m: this function set the initial condition in the domain.
3. boundary_condition.m: this function controls that the boundary conditions imposed in the domain remain univariant.
4. source_term.m: it contains the source term (S) of the Euler equation (Eq. 2.17).
5. WENO5LF2d_sim.m: in this function WENO numerical method is implemented with 5th order scheme, Lax-Friedrichs flux splitting, 2 dimension and symmetric.

1. main_WENO.m

```
%% WENO (Weighted Essentially Non-Oscillatory)
% This is the main program to solve the supersonic jet of a micro-nozzle
% using a numerical approach based in WENO and Runge-Kutta 4 step (time
% depended). This program with all the function will solve the Euler
% equation: dW/dt + dF/dx + dG/dy + alpha*S = 0
% where alpha = 0 for 2D and alpha = 1 for axisymmetric nozzle
%     |   rho   |      |   rho * u   |       |   rho * v   |       |   rho * v     |
%     |rho * u  |      | rho * u^2 + p |     | rho * u * v |       | rho * u * v   |
% W = |rho * v  | F = | rho * u * v  | G = | rho * v^2 + p | S=1/y|   rho * v^2   |
%     |   e     |      |  (e + p)*u  |       |  (e + p)*v  |       |   (e + p)*v   |
% The program is going to be solved dimensionlessly taking as reference the
% exit values. The meaning of the index are : a: atmosphere, e: nozzle
% exist, d: dimensionless
clc; clear; close all;
global gamma ue rhoe pe rhoa pa D
%% Data
% Parameters
alpha    = 1;   % Alpha = 0 (2D). Alpha = 1 (axisymmetric)
gamma    = 1.4; % Heat constant
CFL      = 0.4; % CFL number 0.2-0.4 (Courant-Friedrichs-Levy number)
tFinal   = 125; % Final time
nEx      = 650; % Number of cells in x
nEy      = 150; % Number of cells in y

% Variables
%Dimensionless variables will be calculate using ue,rhoe and D.
rhoe = 1.86;   %Exit density
pe   = 138000; %110300; % Exist pressure
rhoa = 1.2;      % Atmosphere density
pa   = 101300; % Atmosphere pressure
D    = 1000e-6;% Diameter [m]
ue   = 1.709*sqrt(gamma*pe/rhoe); %538.65; %Exit axial velocity 1.709*sqrt(gamma*pe/rhoe)

%% Discretize spatial domain (dimensionless)
% The x domain must be at least 30 times the diameter.
% The y domain must be at leas 5 times the diameter.
a=0; b=30; dx=(b-a)/nEx; nx=nEx+1; x=linspace(a,b,nx);
c=0; d=5; dy=(d-c)/nEy; ny=nEy+1; y=linspace(c,d,ny);
[Y,X] = meshgrid(y,x);

%% Initial condition
[q0,aref,bref1,bref2] = initial_condition(X,Y);
t    = 0; % Time of the calculation
it   = 0; % Iteration number
cont = 1; % Counter (number of data saved)
cont2= 1; % Counter 2 *number of data saved over time = 100
%Matrix inicialization
jacF     = zeros(nx,ny,7);
jacG     = jacF;
Sy       = zeros(nx,ny,4);
% If we want to start the calculation from a prior calculation change the
% number 0 for 1.
if 0 == 1
    load('AS_NPR5_it_20.mat','q','t');
    q = boundary_condition(q,q0,aref,bref1,bref2);
    q0=q;
    cont  = 1;
    cont2 = 1;
end
```

```matlab
%% Time domain
lambda=ue/ue+sqrt(gamma*(pe/(rhoe*ue^2))/(rhoe/rhoe)); % Maximum of the values
dt=CFL*dx/lambda;   % using the system's largest eigenvalue
q = q0;
lambdaF = lambda;
lambdaG = lambda;

%% Solver loop
%Representation of the initial condition
figure;
cla;contourf(X,Y, q0(:,:,1),20);title(['t/(D/ue) =' num2str(t)]); colorbar;
xlabel('x/D')
ylabel('y/D')
pause(0.0001)

while t<tFinal
    % Runge-Kutta 4 step, time calculation
    qo = q;
    % 1st step
    dF = WENO5LF2d_sim(lambdaF,qo,dx,1); %Fx
    dG = WENO5LF2d_sim(lambdaG,qo,dy,2); %Gy
    if alpha == 1
        Sy = source_term(qo, Y); %S
    end
    LW = dF+dG+Sy;
    q1 = qo-0.5*dt*LW;

    q1 = boundary_condition(q1,q0,aref,bref1,bref2);

    % 2nd Step
    dF = WENO5LF2d_sim(lambdaF,q1,dx,1);
    dG = WENO5LF2d_sim(lambdaG,q1,dy,2);
    if alpha == 1
        Sy = source_term(q1, Y);
    end
    LW = dF+dG+Sy;
    q2 = qo-0.5*dt*LW;

    q2 = boundary_condition(q2,q0,aref,bref1,bref2);

    % 3rd Step
    dF = WENO5LF2d_sim(lambdaF,q2,dx,1);
    dG = WENO5LF2d_sim(lambdaG,q2,dy,2);
    if alpha == 1
        Sy = source_term(q2, Y);
    end
    LW = dF+dG+Sy;
    q3 = qo-dt*LW;

    q3 = boundary_condition(q3,q0,aref,bref1,bref2);

    % 4th stage
    dF = WENO5LF2d_sim(lambdaF,q3,dx,1);
    dG = WENO5LF2d_sim(lambdaG,q3,dy,2);
    if alpha == 1
        Sy = source_term(q3, Y);
    end
    LW = dF+dG+Sy;
    q  = 1/3*(-qo+q1+2*q2+q3)-1/6*dt*LW;

    q  = boundary_condition(q,q0,aref,bref1,bref2);

    % Compute primary dimensionless properties
    rhod =   q(:,:,1);        % Dimensionless density
    ud   =   q(:,:,2)./rhod; % Dimensionless axial velocity
    vd   =   q(:,:,3)./rhod; % Dimensionless radial velocity
    ed   =   q(:,:,4);        % Dimensionless energy
    pd   =   (gamma-1)*(ed-0.5*rhod.*(ud.^2+vd.^2)); %Dimensionless pressure

    % Jacobian matrix calculation for F and G
    ud2 = ud.^2;
    vd2 = vd.^2;
    jacF(:,:,1) = 1.6*ud2-0.4*vd2;
    jacF(:,:,2) = 1.6*ud;
    jacF(:,:,3) = 1.6*vd;
    jacF(:,:,4) = 2*ud.*vd;
    jacF(:,:,5) = 2*gamma*ed.*ud./rhod-ud2.*ud-ud2.*vd;
    jacF(:,:,6) = gamma*ed./rhod-1.5*ud2-ud.*vd;
    jacF(:,:,7) = 0.5*ud2;

    jacG(:,:,1) = 1.6*vd2-0.4*ud.^2;
    jacG(:,:,2) = jacF(:,:,3);
    jacG(:,:,3) = jacF(:,:,2);
    jacG(:,:,4) = jacF(:,:,4);
    jacG(:,:,5) = 2*gamma*ed.*vd./rhod-vd2.*vd-vd2.*ud;
    jacG(:,:,6) = gamma*ed./rhod-1.5*vd2-vd.*ud;
    jacG(:,:,7) = 0.5*vd2;
    lambdaF = max(max(max(jacF)));
```

```matlab
    lambdaG = max(max(max(jacG)));

    %Time update and counter
    dt = real(CFL/(max(max(ud))/dx+max(max(vd))/dy));
    t  = t+dt;
    it = it+1;

    %Plotting and saving
    if mod(it,50)==0
        cla;contourf(X,Y, q(:,:,1),20);title(['t/(D/ue) =' num2str(t)]); colorbar;
        pause(0.00001)
    end

    if mod(it,200)==0 && t < 100
        conts = num2str(cont);
        file = strcat('AS_NPR5_it_',conts);
        save(file,'q','t');
        cont = cont+1

    elseif mod(it,50)==0 && t >= 100

        conts2 = num2str(cont2);
        file = strcat('AS_NPR5_t100_it_',conts2);
        save(file,'q','t');
        cont2 = cont2+1

    end

end % t<tFinal
```

2. initial_condition.m

```matlab
function [q0,aref,bref1,bref2] = initial_condition(X,Y)
% This function will create the initial condition q0 of the flux. Also, it
% will obtain the parameters aref, bref1 and bref2 for reference in the
% boundary condition.

%INPUT
%X -> x values of the mesh
%Y -> y values of the mesh
%OUTPUT
%q0   -> initial value of the flow field
%aref -> x cell where the nozzle end
%bref1-> y cell where the nozzle start
%bref2-> y cell where the nozzle end

global gamma ue rhoe pe rhoa pa D

[m,n] = size(X);
q0    = zeros(m,n,4);


a    = find(X(:,1)  <= D/D );
b    = find(Y(1,:)  <= (D/D)/2);
aref = a(end);
bref2= b(end);
bref1= 1;%round(n/2 -(bref2-n/2));

% Atmosphere condition
q0(:,:,1) = rhoa/rhoe;
q0(:,:,4) = (pa/(gamma-1))/(rhoe*ue^2);

% Exit condition
q0(1:aref,bref1:bref2,1) = rhoe/rhoe; %rho
q0(1:aref,bref1:bref2,2) = rhoe*ue/(rhoe*ue); %rho * u
q0(1:aref,bref1:bref2,4) = (pe/(gamma-1)+0.5*rhoe*(ue^2))/(rhoe*ue^2); %e

end
```

3. boundary_condition.m

```matlab
function q = boundary_condition(q,q0,aref,bref1,bref2)
% This function will imposse the boundary condition to the flow field.
% The matrix q contain the last flow field calculated and the q0
% contains the condition which must be impossed in the flow field
%INPUT
%q    -> flow field
%q0   -> initial value of the flow field
%aref -> x cell where the nozzle end
%bref1-> y cell where the nozzle start
%bref2-> y cell where the nozzle end
```

```
%OUTPUT
%q    -> corrected flow field

q(1:aref,bref1:bref2,:)   = q0(1:aref,bref1:bref2,:);    %B1
q(1:aref,bref2:bref2+1,:) = q0(1:aref,bref2:bref2+1,:);  %B2
q(1,bref2:end,:)          = q0(1,bref2:end,:);           %B3
q(:,end,:)                = q0(:,end,:);                 %B4
q(:,1,3)                  = q0(:,1,3);                   %B5
q(end,:,:)                = q0(end,:,:);                 %B6
end
```

4. source_term.m

```
function Sy = source_term(q, Y)
% This function calculate the source term of the Euler equation
% INPUT
% q  -> flow field
% Y  -> y values of the mesh
% OUTPUT
% Sy -> Source term
    global gamma

    [m,n,~] = size(q);

    invY = (1./Y);

    Sy = zeros(m,n,4);
    Sy(:,:,1) = invY.*q(:,:,3);

    rho=q(:,:,1); u=q(:,:,2)./rho; v=q(:,:,3)./rho;
    e=q(:,:,4); p=(gamma-1)*(e-0.5*rho.*(u.^2+v.^2));

    Sy(:,:,2) = invY.*rho.*u.*v;
    Sy(:,:,3) = invY.*rho.*v.^2;
    Sy(:,:,4) = invY.*(e+p).*v;

    if mod(n,2)~=0
        Sy(:,1,:) = 0;
    end

end
```

5. WENO5LF2d_sim.m

```
function dFx = WENO5LF2d_sim(lambda,q,dx,dir)
% This function will solve a flux field step using the WENO numerical
% method. The function solve symmetric field over the x-axis in 2D.
% INPUT
% a  -> Lax-Friedrich splitting flux constant
% q  -> flow parameters
% dx ->
% dir-> diraction of the method. dir = 1 is for dF and dir = 2 is for dG.
% OUTPUT
% dFx-> d(flux)/dx
%
% Domain cells (I{i}) reference:
%
%                  |           |   u(i)      |             |
%                  |   u(i-1)  |_____|             |
%                  |_____|             |   u(i+1)    |
%                  |           |             |_____|
%           ...|-----o-----|-----o-----|-----o-----|...
%                  |    i-1    |     i      |    i+1      |
%                  |-          +|-          +|-          +|
%              i-3/2        i-1/2        i+1/2        i+3/2
%
% Stencils (S{r}) reference:
%
%
%                                   |_____S2_____|
%                                   |                       |
%                       |_____S1_____|           |
%                       |                       |           |
%           |_____S0_____|           |           |
%         ..|---o---|---o---|---o---|---o---|---o---|...
%           | I{i-2}| I{i-1}|  I{i} | I{i+1}| I{i+2}|
%                                   -|
%                                  i+1/2
%
%
```

```matlab
%                    |_____S0_____|
%                    |                          |
%                    |         |_____S1_____|
%                    |         |                          |
%                    |         |          |_____S2_____|
%                  ..|---o---|---o---|---o---|---o---|---o---|...
%                    | I{i-2}| I{i-1}|  I{i} | I{i+1}| I{i+2}|
%                                    |+
%                                   i-1/2
%
%% Flux calculation
global gamma
% primary properties
rho=q(:,:,1); u=q(:,:,2)./rho; v=q(:,:,3)./rho; e=q(:,:,4)./rho;
p=(gamma-1)*rho.*(e-0.5*(u.^2 + v.^2));
flux = zeros(size(q));
% Flux vector of conserved properties
if dir == 1
    flux(:,:,1)= rho.*u;
    flux(:,:,2)= rho.*u.^2+p;
    flux(:,:,3)= rho.*u.*v;
    flux(:,:,4)= u.*(rho.*e+p);
    turn=[1 0 0];
elseif dir == 2
    flux(:,:,1)= rho.*v;
    flux(:,:,2)= rho.*u.*v;
    flux(:,:,3)= rho.*v.^2+p;
    flux(:,:,4)= v.*(rho.*e+p);
    turn=[0 1 0];
end

%% Lax-Friedrich splitting flux separation (right)
fr=0.5*(flux+lambda*q);

% Right Flux
% Shift of the flux to place the variables of the Stencils in the same cell
frm2 = circshift(fr, 2*turn); %flux_right_minus_2
frm1 = circshift(fr,   turn); %flux_right_minus_1
frp1 = circshift(fr,-1*turn); %flux_right_plus_1
frp2 = circshift(fr,-2*turn); %flux_right_plus_2

if dir == 2 %Symmetry condition imposed only for y direction
    frm2(:,2,:)    = frm2(:,4,:);     frm2(:,1,:)   = frm2(:,5,:);
    frm1(:,1,:)    = frm1(:,3,:);
    frp1(:,end,:)  = frp1(:,end-1,:);
    frp2(:,end-1,:)= frp2(:,end-2,:); frp2(:,end,:) = frp2(:,end-3,:);
    % Radial speed must have the oposite sign
    frm2(:,2,3) = -frm2(:,4,3); frm2(:,1,3) = -frm2(:,5,3);
    frm1(:,1,3) = -frm1(:,3,3);
end

% Stencils
S0r = (2*frm2 - 7*frm1 + 11*fr)/6;
S1r = ( -frm1 + 5*fr   + 2*frp1)/6;
S2r = (2*fr   + 5*frp1 - frp2 )/6;
% Smooth Indicators (Stencil interpolation)
IS0r = 13/12*(frm2 - 2*frm1 + fr  ).^2 + 1/4*(frm2 - 4*frm1 + 3*fr).^2;
IS1r = 13/12*(frm1 - 2*fr   + frp1).^2 + 1/4*(frm1 - frp1   ).^2;
IS2r = 13/12*(fr   - 2*frp1 + frp2).^2 + 1/4*(3*fr - 4*frp1 + frp2).^2;
% Optimal weight
C0r = 1/10; C1r = 6/10; C2r = 3/10;
epsilon = 1e-6; %Small number to avoid /0
% omega weights
w0r = C0r./(epsilon + IS0r).^2;
w1r = C1r./(epsilon + IS1r).^2;
w2r = C2r./(epsilon + IS2r).^2;
wsumr = w0r + w1r + w2r;
% stencils weigths
sw0l = w0r./wsumr;
sw1l = w1r./wsumr;
sw2l = w2r./wsumr;

% Numerical Flux at cell boundary
hr = sw0l.*S0r + sw1l.*S1r + sw2l.*S2r; %flux_(i+1/2)^[+]

%% Lax-Friedrich splitting flux separation (left)
%fl=0.5*(flux-lambda*q);
flm1 = 0.5* (flux-lambda*q); %flux_left_minus_1

flm2 = circshift(flm1,   turn); %flux_left_minus_2
fl   = circshift(flm1,-1*turn); %Lax-Friedrich splitting flux separation (left)
flp1 = circshift(flm1,-2*turn); %flux_left_plus_1
flp2 = circshift(flm1,-3*turn); %flux_left_plus_1

if dir == 2 %Symmetry condition imposed only for y direction
    flm2(:,1,:) = flm2(:,3,:);
    fl(:,end,:) = fl(:,end-1,:);
    flp1(:,end-1,:) = flp1(:,end-2,:); flp1(:,end,:)   = flp1(:,end-3,:);
```

```matlab
    flp2(:,end-2,:) = flp2(:,end-3,:); flp2(:,end-1,:) = flp2(:,end-4,:); flp2(:,end,:) = flp2(:,end-
5,:);
    %Radial speed must have the oposite sign
    flm2(:,1,3) = -flm2(:,3,3);
end

% Stencils
S0l = (  -flm2 + 5*flm1 + 2*fl  )/6;
S1l = ( 2*flm1 + 5*fl   - flp1  )/6;
S2l = (11*fl   - 7*flp1 + 2*flp2)/6;
% Smooth Indicators (Stencil interpolation)
IS0l = 13/12*(flm2 - 2*flm1 + fl  ).^2 + 1/4*(flm2 - 4*flm1 + 3*fl).^2;
IS1l = 13/12*(flm1 - 2*fl   + flp1).^2 + 1/4*(flm1 -   flp1 ).^2;
IS2l = 13/12*(fl   - 2*flp1 + flp2).^2 + 1/4*(3*fl - 4*flp1 + flp2).^2;
% Optimal weight
C0l = 3/10; C1l = 6/10; C2l = 1/10;
% omega weights
w0l = C0l./(epsilon + IS0l).^2;
w1l = C1l./(epsilon + IS1l).^2;
w2l = C2l./(epsilon + IS2l).^2;
wsuml = w0l + w1l + w2l;
% ENO stencils weigths
sw0l = w0l./wsuml;
sw1l = w1l./wsuml;
sw2l = w2l./wsuml;

% Numerical Flux at cell boundary
hl = sw0l.*S0l + sw1l.*S1l + sw2l.*S2l; %flux_(i+1/2)^[-]

%% Compute finite volume residual term, df/dx.
hll = circshift(hl,turn); %flux_(i-1/2)^[-]
hrr = circshift(hr,turn); %flux_(i-1/2)^[+]

if dir == 2 %Symmetry condition imposed only for y direction
    hll(:,1,:) = hll(:,3,:);
    hrr(:,1,:) = hrr(:,3,:);
    % Radial speed must have the oposite sign
    hll(:,1,3) = -hll(:,3,3);
    hrr(:,1,3) = -hrr(:,3,3);
end

dFx = ((hr+hl)-(hrr+hll))/dx; %dF/dx
end
```

Appendix 3. Prandtl model code

The code implemented to simulate the Prandtl's model is displayed below. The pressure of the jet can be obtained as follow:

$$p(x) = p_b + \sum_{i=1}^{n\_modes} p_s(mode_i)$$

Eq. 0.1

Where p_b is the atmosphere pressure and n_modes is the number of modes obtained.

In Figure 0.1 the first 6 oscillation modes of the Prandtl's model are calculated. We can observe when the mode is higher the amplitude is smaller; and therefore, its contribution to the solution.
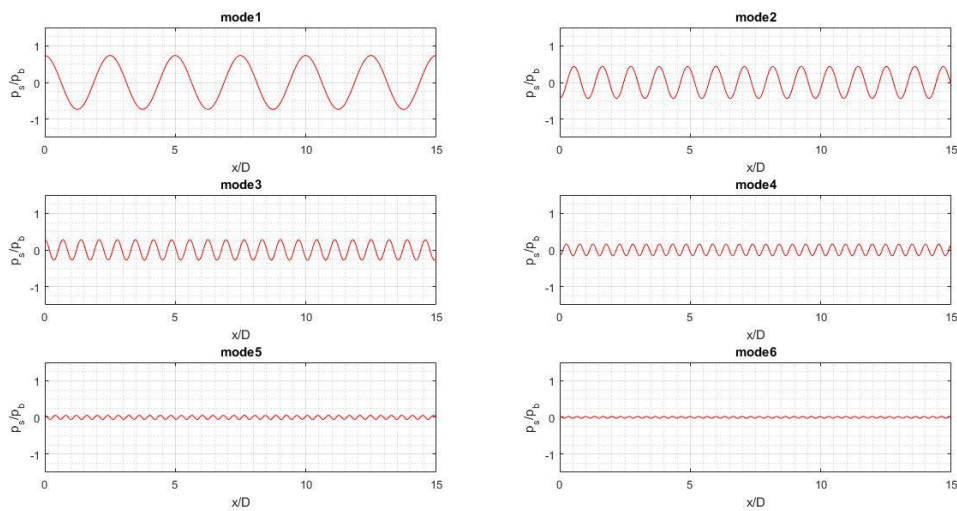

Figure 0.1. 6 oscillation modes of Prandtl model.

Figure 0.2. shows the solution of the Prandtl model when 6 modes are used in the representation. This solution is compared with the first mode. We can see the 1st mode has the bigger contribution to the solution, so the trend of the solution can be observed using exclusively this mode. Even though the whole solution is given by the summation of the modes, in Section 4 only the 1st mode is represented since the objective is to observe the trend of the pressure.
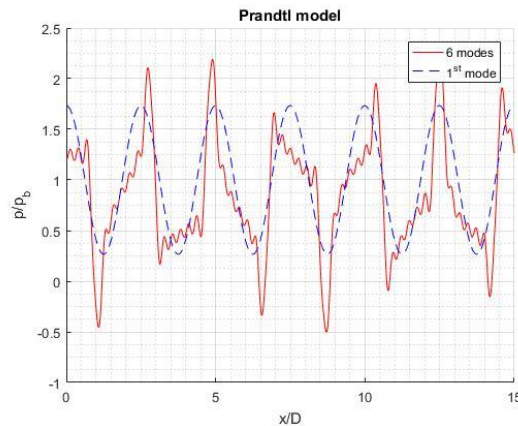

Figure 0.2. Representation of the Prandtl model using 6 oscillation modes.

Three different function are used:

1. ps.m: which contain the Prandtl's model and calculate the value of ps.
2. besselzero.m: finds the roots of the Bessel functions.
3. findzero.m: Halley's method.

1. ps.m

```matlab
function [modes,x] = ps(n_modes, n_values, number_diameter, r, D, Dj, Md, Mj, rhoj, gamma, R, Pb)
%  The objective of this function is to calculate the pressure Ps using the
%  mathematical model of Prandtl. A multiple-scales model of the shock-cell
%  structure of imperfectly expanded supersonic jets.
%  The solution is a matrix which each column represent a mode.
% INPUT
% n_modes         -> Number of modes to be calculated
% n_values        -> Number of values to be obtained per mode
% number_diameter -> Number of diameter in x-axis which want to be represented
% r               -> Radial position
% D               -> Diameter
% Dj              -> Fully expanded diameter
% Md              -> Design Mach
% Mj              -> Fully expanded Mach
% rhoj            -> Fully expanded density
% gamma           -> Heat capacity ratio
% R               -> Gas constant
% Pb              -> Atmosphere pressure
% OUTPUT
% mode            -> Matrix which contain in each column a vibration mode
% x               -> x discretitation

x = linspace(0, number_diameter*D, n_values); %x discretitation
modes = zeros(n_modes, n_values); %matrix initialization
Pj = Pb; %Assuming fully expanded pressure is ambient pressure
Tj = Pj/(rhoj*R); %Perfect gas equation
Uj=Mj*sqrt(gamma*R*Tj); % Mach and sonic speed definition

DP=(rhoj*Uj^2)*1/(gamma*Mj^2)*(((1+1/2*(gamma-1)*Mj^2)/(1+1/2*(gamma-1)*Md^2))^(gamma/(gamma-1))-1);
%Prandtl

Bessel_roots=besselzero(0,n_modes,1); %Function which obtain the Bessel roots.

for i = 1:n_modes

    Ai = 2* DP*D/Dj*besselj(1,Bessel_roots(i)*D/Dj)/(Bessel_roots(i)*besselj(1,Bessel_roots(i))^2);
%Prandtl

    modes(i,:) = Ai * besselj(0,2*Bessel_roots(i)*r/Dj) * cos(2*Bessel_roots(i)*x/(Dj*sqrt(Mj^2-1)));
%Prandtl

end
%end Ps
```

2. besselzero.m

```matlab
function vector_zeros=besselzero(n,k,kind)
% Find first k positive zeros of the Bessel function J(n,x) or Y(n,x)
% using Halley's method.

k3=3*k;

vector_zeros=zeros(k3,1);

for j=1:k3

    % Initial guess of zeros
    x0=1+sqrt(2)+(j-1)*pi+n+n^0.4;

    % Do Halley's method
    vector_zeros(j)=findzero(n,x0,kind);

end

vector_zeros=sort(vector_zeros);
dx=[1;abs(diff(vector_zeros))];
vector_zeros=vector_zeros(dx>1e-8);

vector_zeros=vector_zeros(1:k);
%end besselzero
```

3. findzero.m

```matlab
function x=findzero(n,x0,kind)

n1=n+1;

% Tolerance
tol=1e-12;

% Maximum number of times to iterate
MAXIT=100;

% Initial error
err=1;

iter=0;

while abs(err)>tol && iter<MAXIT

    switch kind
        case 1
            a=besselj(n,x0);
            b=besselj(n1,x0);
        case 2
            a=bessely(n,x0);
            b=bessely(n1,x0);
    end

    x02=x0*x0;

    err=2*a*x0*(n*a-b*x0)/(2*b*b*x02-a*b*x0*(4*n+1)+(n*n1+x02)*a*a);

    x=x0-err;
    x0=x;
    iter=iter+1;

end
%end findzero
```